

# Relationships of Rainy Season Precipitation and Temperature to Climate Indices in California: Long-Term Variability and Extreme Events

YI-CHIN LIU AND PINGKUAN DI

*Air Resources Board, California Environmental Protection Agency, Sacramento, California*

SHU-HUA CHEN

*Department of Land, Air and Water Resources, University of California, Davis, Davis, California*

JOHN DAMASSA

*Air Resources Board, California Environmental Protection Agency, Sacramento, California*

(Manuscript received 5 June 2017, in final form 4 December 2017)

## ABSTRACT

To better understand the change in California's climate over the past century, the long-term variability and extreme events of precipitation as well as minimum, mean, and maximum temperatures during the rainy season (from November to March) are investigated using observations. Their relationships to 28 rainy season average climate indices with and without time lags are also studied. The precipitation variability is found to be highly correlated with the tropical/Northern Hemisphere pattern (TNH) index at zero time lag with the highest correlation in Northern California and the Sierra and the correlation decreasing southward. This is an important finding because there have been no conclusive studies on the dominant climate modes that modulate precipitation variability in Northern California. It is found that the TNH modulates California precipitation variability through the development of a positive (negative) height anomaly and its associated low-level moisture fluxes over the northeast Pacific Ocean during the positive (negative) TNH phase. Temperature fields, especially minimum temperature, are found to be primarily modulated by the east Pacific/North Pacific pattern, Pacific decadal oscillation, North Pacific pattern, and Pacific–North American pattern at zero time lag via changes in the lower-tropospheric temperature advections. Regression analysis suggests a combination of important climate indices would improve predictability for precipitation and minimum temperature statewide and subregionally compared to the use of a single climate index. While California's precipitation currently is primarily projected by ENSO, this study suggests that using the combination of the TNH and ENSO indices results in better predictability than using ENSO indices only.

## 1. Introduction

Climate variability in California has been demonstrated to be significantly modulated by atmospheric and oceanic modes/patterns through their influence on atmospheric circulations, based on both observational and

numerical studies (Fierro 2014; Wang et al. 2014; Higgins et al. 2007; Gershunov and Barnett 1998; Wise 2010; Kam and Sheffield 2016; Carrillo et al. 2017). The climate variability in California reflects large fluctuations in temporal and spatial scales for both precipitation and temperature. For example, California received about 180% of a normal year's averaged precipitation from 1994 to 1995, yet only received 30%–40% of annually averaged precipitation from 2011 to 2015. California's climate variability is also greatly impacted by its complex topography and broad latitudinal extent, leading to a wide spectrum of climates and large differences in annual precipitation and average temperature among different geographic regions (Abatzoglou et al. 2009; Guttman and Quayle 1996). For example, Northern California can

---

Denotes content that is immediately available upon publication as open access.

---

Supplemental information related to this paper is available at the Journals Online website: <https://doi.org/10.1175/JCLI-D-17-0376.s1>.

---

Corresponding author: Yi-Chin Liu, [karry.liu@arb.ca.gov](mailto:karry.liu@arb.ca.gov)

DOI: 10.1175/JCLI-D-17-0376.1

© 2018 American Meteorological Society. For information regarding reuse of this content and general copyright information, consult the [AMS Copyright Policy](#) ([www.ametsoc.org/PUBSReuseLicenses](http://www.ametsoc.org/PUBSReuseLicenses)).

receive 2 to 4 times more precipitation than Southern California in a normal year (Jones 2000).

Many atmospheric and oceanic modes exhibit persistent and recurring large-scale patterns with various temporal and spatial scales. Among those modes, El Niño–Southern Oscillation (ENSO), the Pacific decadal oscillation (PDO), the North Atlantic Oscillation (NAO), and the Arctic Oscillation (AO) have been extensively investigated as a link to the climate variability in precipitation and temperature over the southwest United States, including California, Nevada, and Arizona (Schonher and Nicholson 1989; Fierro 2014; Higgins et al. 2007; Gershunov and Barnett 1998; Mo et al. 2009; Mo and Higgins 1998; Hoell et al. 2016; Kam and Sheffield 2016; Zhu and Li 2016, 2018). ENSO is one of the climate modes that has received the most attention when correlating to California precipitation variabilities. For example, the Climate Prediction Center (CPC) has used ENSO as a primary predictor for their seasonal forecasts whether California would experience wetter or drier weather conditions (Wise et al. 2015). Most of the studies agree that ENSO has a substantial influence on precipitation in Southern California. However, the impact of ENSO on central and Northern California is not yet conclusive (Abatzoglou et al. 2009). Some studies suggested that ENSO has very little effect on central and Northern California precipitation (Becker et al. 2009; Schonher and Nicholson 1989; Mo and Higgins 1998; Fierro 2014), while some studies suggested otherwise (Hoell et al. 2016). For example, Schonher and Nicholson (1989) found that precipitation over central California could be both above or below normal during El Niño events, and the precipitation over the Sierra Nevada and Northern California has little correlation to ENSO. Similar results were obtained by Fierro (2014) showing that ENSO had the maximum impact on the rainy season average (from October to April) precipitation over Southern California and the impact significantly decreases northward. A recent study conducted by Hoell et al. (2016) found that California precipitation is sensitive to El Niño intensity. A higher wet probability may occur during strong El Niño events across the entire state, but precipitation in Northern California shows no significant differences between weak and moderate El Niño events.

The PDO is one of the dominant modes for decadal variability over the Pacific Ocean that represents signals from a combination of remote tropical modes and local North Pacific air–sea interactions (Newman et al. 2016). Previous studies suggested that the PDO would have little direct impact on precipitation and temperature over the southwest United States but can have indirect influences on the regions through the modulation of

ENSO effects or other internal variability of the mid-latitude atmosphere (Gershunov and Barnett 1998; McCabe and Dettinger 1999; Mo et al. 2009; Mills and Walsh 2013; Newman et al. 2016). For example, a recent study by Liu et al. (2016) found that the PDO can influence California precipitation through the modification of the frequency and intensity of atmospheric rivers (ARs), a large-scale process that is often linked to extreme rainfall events in California.

The NAO is the major large-scale mode of atmospheric variability over the extratropical Atlantic Ocean. Although the NAO has been considered to have very small effects over the western United States (Hurrell and van Loon 1997; Higgins et al. 2000; Panagiotopoulos et al. 2002; Whan and Zwiers 2017), recent studies by Myoung et al. (2015, 2017) suggested otherwise. Myoung et al. (2017) found that snowmelt period and timings of snowmelt in California, Nevada, Utah, and Colorado are highly related to the NAO. Myoung et al. (2015) found a substantial linkage between the NAO and surface air temperatures over the southwest United States during the March–June period, and the linkage has become stronger in the last 30-yr period (1980–2009) compared to the previous 30-yr period (1950–79). They pointed out that the NAO modulated the location of upper-tropospheric anticyclones over the western United States, causing changes to lower-tropospheric wind directions, suppressing precipitation, and increasing shortwave radiation at the surface. These led to the change of air temperatures over the southwest United States.

The AO is the dominant mode of variability in the atmospheric pressures for the Arctic and North Atlantic oceans and has a very wide temporal spectrum with the largest effect in the winter (Thompson and Wallace 1998). Because the AO covers a large part of the North Atlantic Ocean, the AO often shares the same oscillation phase with the NAO and sometimes causes similar effects as the NAO on weather across the United States. It has been found that California tends to experience drier (wetter) weather conditions at AO positive (negative) phases (McAfee and Russell 2008; McCabe-Glynn et al. 2016). It has been suggested that the AO variability is related to the recent severe drought in California (Wang et al. 2014).

Except for the aforementioned climate modes that have been more frequently studied, the linkages between other climate modes and weather conditions over the southwest United States, in particular over California, are rarely studied. Many prominent Northern Hemisphere teleconnection patterns, such as the Pacific–North American pattern (PNA), the east Atlantic pattern (EA), the west Pacific pattern (WP), the east Pacific/North Pacific pattern (EPNP), the tropical/

Northern Hemisphere pattern (TNH), and the polar/Eurasian pattern (PE), have exhibited important physical and dynamical features (Barnston and Livezey 1987; Wettstein and Wallace 2010; Cayan and Redmond 1994; Wise et al. 2015). However, these patterns have received relatively little attention regarding their potential connections to climate variabilities in California. As there is still no consensus on what climate modes dominate the precipitation and temperature variabilities in Northern California, there is a need to evaluate the linkage between California precipitation and temperature to not only the frequently studied climate modes but also the rarely studied ones.

California produces half of the nation's fruits and vegetables, which makes it the most important agricultural state in the United States. The water supply in California heavily relies on accumulated snowpack over high mountains from previous winter storms and ARs. Thus, California is extremely vulnerable to global and regional climate changes because they can amplify fluctuations in California precipitation amounts and temperature, such as the severe drought during 2011–14. Furthermore, California has a very diverse topography, and each of the different types of topographies responds differently to climate change. This makes the impact of climate change on California more unpredictable compared to other parts of the country. As a result, documenting the spatial and temporal scales in precipitation and temperature and understanding the underlying mechanisms for the state as a whole as well as for its distinct geographic regions are crucial to water resources planning and ongoing climate-related policy and regulation making in California. The objectives of this study are 1) to better understand how long-term rainy season average precipitation, mean temperature, minimum temperature, and maximum temperature have changed over the past century for the whole state and its 11 geographical subregions; 2) to conduct statistics on correlations of precipitation, mean temperature, minimum temperature, and maximum temperature to a comprehensive set of large-scale climate indices for the whole state and its 11 geographical subregions; 3) to investigate the predictability of California precipitation and temperature using significantly correlated climate indices; and 4) to explore the mechanisms underlying the relationships of precipitation and temperature to climate indices.

## 2. Data and methodology

### a. Data

The time series data of monthly accumulated precipitation, average maximum temperature, average mean

temperature, and average minimum temperature from 1895 to 2015 used in this study are obtained from the California Climate Tracker (<http://www.wrcc.dri.edu/monitor/cal-mon/>; Abatzoglou et al. 2009). Monthly average mean temperature is retrieved from the average of daily mean temperature, which is the average of daily maximum and minimum temperatures. The dataset of the above precipitation and temperature is specifically created for California using a total of 195 stations across California from the National Weather Service Cooperative Observer Network (COOP) along with gridded data from the Parameter-Elevation Relationships on Independent Slopes Model (PRISM) database. In addition to the statewide (CAL) data that are available in the dataset, data from 11 geographical regions in California were also available: North Coast (A), North Central (B), Northeast (C), Sierra (D), Sacramento Delta (E), Central Coast (F), San Joaquin Valley (G), South Coast (H), South Interior (I), Mojave Desert, and Sonoran Desert (K) (Fig. 1). The 11 subregions are divided based on their geographic features and regional climate variabilities (Abatzoglou et al. 2009).

The majority of the annual rainfall in California occurs from November through March [Fig. S1 in the supplemental information (SI)], which is defined as California's rainy season in this study. The rainy season average detrended monthly accumulated precipitation anomalies  $P_{\text{avg}}$ , maximum temperature anomalies  $T_{\text{max}}$ , mean temperature anomalies  $T_{\text{avg}}$ , and minimum temperature anomalies  $T_{\text{min}}$  are used for most of the analyses conducted in this study. To calculate each monthly anomaly, we subtract the monthly average based on the 1981–2010 period from each monthly data. After that, we detrend the monthly anomaly data, and then take the average of the detrended anomaly data for the months of November to March, for each year.

Gridded monthly atmospheric data, including geopotential heights, winds, total cloud coverage, and cloud forcing net longwave and shortwave fluxes at the surface, are obtained from NCEP–NCAR reanalysis datasets (Kalnay et al. 1996). The data are downloaded from the Earth System Research Laboratory (ESRL) Physical Sciences Division (PSD; <http://www.esrl.noaa.gov/psd/data/gridded/data.ncep.reanalysis.derived.pressure.html>). Similar to the land-based data described above, the anomalies are calculated with respect to the 1981–2010 period and then detrended and averaged from November to March to become a rainy season average detrended dataset.

To explore possible relationships of individual climate indices and/or their combination to California precipitation and temperature in the rainy season, a large set of climate indices (a total of 28) is used in this study

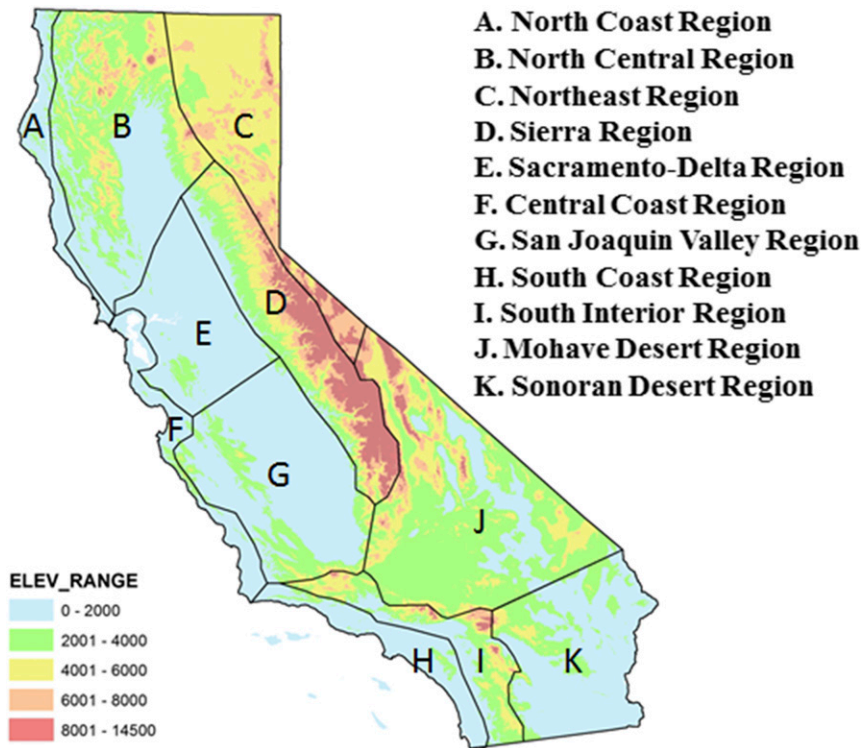


FIG. 1. The 11 subregions (A–K) across the state of California in the dataset from the California Climate Tracker. Shading indicates the local elevation in feet.

(see Table 1 for abbreviations and acronyms and Table S1 in the SI for detailed descriptions). These climate indices include 12 ENSO-related indices, 4 Atlantic Ocean-related indices, 2 Pacific Ocean-related indices, 7 teleconnection-related indices, and 3 atmosphere-related indices. All 28 climate indices are monthly data initially and are averaged from November to March to become rainy season average climate indices. Please note that the TNH index is only available from December to February. Therefore, the rainy season average values of the TNH index are represented by the December–February mean values. Hereafter, “rainy season average” for climate indices will be omitted for the sake of brevity.

ENSO is a large, convoluted, and dynamic system, and its effects on weather and climate vary from one location to another. Thus, it is believed that using several different indices can be informative and beneficial in measuring and monitoring the ENSO state. In this study, we use 12 of them from the literature (Trenberth 1984; Wolter and Timlin 1993, 1998, 2011; Ashok et al. 2007; Weng et al. 2007, 2009; Trenberth and Stepaniak 2001), including the Southern Oscillation index (SOI), the multivariate ENSO index (MEI), 8 SSTA-based ENSO indices [Niño-1+2, Niño-3.4, Niño-3, Niño-4, El Niño

Modoki A, El Niño Modoki B, El Niño Modoki C, and El Niño Modoki (EMI)], the Trans-Niño index (TNI), and the Oceanic Niño index (ONI).

Many studies have found the cross-basin interaction between the Atlantic and Pacific Oceans (Wu et al. 2007; Tootle and Piechota 2006), which implies that the modes from the Atlantic Ocean may have a potential influence on California precipitation and temperature. Therefore, four Atlantic Ocean-related indices are selected, including the Atlantic multidecadal oscillation (AMO) index (Schlesinger and Ramankutty 1994; Enfield et al. 2001), tropical North Atlantic (TNA) index (Enfield et al. 1999), tropical South Atlantic (TSA) index, and Western Hemisphere warm pool (WHWP) index (Wang and Enfield 2001). The first three are based on the area average of SSTA but over different regions. WHWP is based on the monthly anomaly of the ocean surface regions warmer than 28.5°C in the Atlantic and eastern North Pacific.

The first Pacific Ocean-related index is the PDO index. The PDO index is positive (negative) when SSTA is cool (warm) in the interior North Pacific and warm (cool) along the Pacific Coast, or when sea level pressure (SLP) is below (above) average over the North Pacific (Mantua et al. 1997). The second Pacific Ocean-related

TABLE 1. Abbreviations and acronyms for 28 climate indices, including 12 ENSO-related indices, 4 Atlantic Ocean-related indices, 2 Pacific Ocean-related indices, 7 teleconnection-related indices, and 3 atmosphere-related indices.

No.	Climate indices
ENSO-related indices	
1	Southern Oscillation (SOI)
2	Multivariate ENSO (MEI)
3	Niño-1+2
4	Niño-3.4
5	Niño-3
6	Niño-4
7	El Niño Modoki A
8	El Niño Modoki B
9	El Niño Modoki C
10	El Niño Modoki (EMI)
11	Oceanic Niño index (ONI)
12	Trans-Niño index (TNI)
Atlantic Ocean-related indices	
13	Atlantic multidecadal oscillation (AMO)
14	Tropical Northern Atlantic (TNA)
15	Tropical Southern Atlantic (TSA)
16	Western Hemisphere warm pool (WHWP)
Pacific Ocean-related indices	
17	Pacific decadal oscillation (PDO)
18	North Pacific Index (NPI)
Teleconnection indices	
19	Pacific-North American pattern (PNA)
20	East Pacific/North Pacific Oscillation (EPNP)
21	Hurrell station-based monthly North Atlantic Oscillation (NAO)
22	East Atlantic pattern (EA)
23	Polar/Eurasia pattern (PE)
24	West Pacific pattern (WP)
25	Tropical/Northern Hemisphere pattern (TNH)
Atmospheric-related indices.	
26	Arctic Oscillation (AO)
27	Quasi-Biennial Oscillation (QBO)
28	Solar flux (Solar)

index is the North Pacific index (NPI), which is used to quantify decadal variations in the atmospheric circulation over the North Pacific Ocean (Trenberth and Hurrell 1994).

Seven teleconnection indices for the Northern Hemisphere extratropics variability are used in this study, including the PNA, EPNP, NAO, EA, PE, WP, and TNH indices (Barnston and Livezey 1987). All of these indices except the NAO index were retrieved from the CPC (<http://www.cpc.ncep.noaa.gov/data/teledoc/telecontents.shtml>). The NAO index used here is the Hurrell NAO index (station based; retrieved from <https://climatedataguide.ucar.edu/climate-data/hurrell-north-atlantic-oscillation-nao-index-station-based>). The six indices from the CPC are based on the six leading

rotated modes obtained by applying the rotated principal component analysis (RPCA) technique to monthly mean standardized 500-mb height anomalies over the region of 20°–90°N with a least squares solution. More details can be found on the CPC website.

The three atmospheric-related indices are the AO index, quasi-biennial oscillation (QBO) index, and solar flux (Solar) index. The AO index is also retrieved from the CPC. The QBO is the dominant mode for the variability in the equatorial stratosphere (Baldwin et al. 2001). The Solar index used in this study is obtained from the National Research Council of Canada. Several studies have shown that solar cycles are correlated to modulation of surface temperature and precipitation (Gray et al. 2010; Maliniemi et al. 2014). For example, significant differences in winter temperature patterns in the North Hemisphere have been found during different phases of the sunspot cycles. It is also suggested that solar cycles might influence the climate precipitation through the solar modulation of galactic cosmic rays or the global electric circuit on cloud cover. There have not yet been any applications of the Solar index to California's climate. We investigate this index to see if solar flux affects California precipitation and temperature.

### b. Methodology

To understand how California precipitation and temperature in the rainy season have changed with time, we perform a long-term trend analysis for rainy season average monthly accumulated precipitation as well as averaged monthly minimum temperature, averaged monthly mean temperature, and averaged monthly maximum temperature using time series data over the past 121 years (1895–2015). Note that for the long-term trend analysis, no anomaly and detrended procedures are performed. A linear regression  $t$  test with 95% confidence interval is used to determine whether the slope of the regression line differs significantly from zero.

The occurrence of extremely dry and wet events is also investigated during the same period. The 5-month standardized precipitation index (SPI) is used to identify different extents of dry and wet scenarios. Extreme wet and dry events are defined as the 5-month SPI above 2 and below  $-2$ , respectively; moderate wet and dry events are from 1 to 2 and from  $-2$  to  $-1$ , respectively; and normal wet and dry events are from 1 to 0 and  $-1$  to 0, respectively (Yoon et al. 2015).

Using a similar approach to that of Fierro (2014), the relationships of California  $P_{\text{avg}}$ ,  $T_{\text{avg}}$ ,  $T_{\text{min}}$ , and  $T_{\text{max}}$  over the whole state and its 11 subregions to the 28 climate indices with and without time lags are investigated using the standard Pearson's method (Wilks 2006). The

statistical significance of the correlations is evaluated using a bootstrap sampling technique over 1000 random samples and is considered as statistically significant when the significance level of the correlation coefficients exceeds 95%. To investigate whether there is a time-lagged correlation of climate indices to  $P_{\text{avg}}$ ,  $T_{\text{avg}}$ ,  $T_{\text{min}}$ , and  $T_{\text{max}}$ , four season lags are considered for the climate indices, including one season ahead [September–October–November (hereafter denoted as  $-1$ )], two seasons ahead [June–July–August ( $-2$ )], three seasons ahead [March–April–May ( $-3$ )], and four seasons ahead [previous year December–January–February ( $-4$ )]. If multiple time lags for one climate index are found to be significantly correlated to  $P_{\text{avg}}$ ,  $T_{\text{avg}}$ ,  $T_{\text{min}}$ , or  $T_{\text{max}}$ , the final time lag for the climate index is determined using the maximum median values of correlation coefficients among contemporaneity and four season lags. Because most of the climate index datasets are only available after 1950, the analyses of relevant correlation statistics are conducted only for the period of 1950–2015.

To examine the predictability of each significantly correlated climate index determined by bootstrapped correlation analyses for  $P_{\text{avg}}$ ,  $T_{\text{avg}}$ ,  $T_{\text{min}}$ , and  $T_{\text{max}}$ , simple linear regression analyses are conducted with individual climate index serving as a predictor variable and either  $P_{\text{avg}}$ ,  $T_{\text{max}}$ ,  $T_{\text{min}}$ , or  $T_{\text{avg}}$  serving as a response variable. In addition, multiple linear regression analyses are also performed to investigate whether any given combinations of significantly correlated climate indices can increase the predictability for  $P_{\text{avg}}$ ,  $T_{\text{max}}$ ,  $T_{\text{min}}$ , and  $T_{\text{avg}}$ . A stepwise regression method is used to develop an optimal regression equation for  $P_{\text{avg}}$ ,  $T_{\text{avg}}$ ,  $T_{\text{min}}$ , or  $T_{\text{max}}$ , which aims to reduce the set of the predictor variables to those that are necessary and account for nearly as much of the variance as is accounted for by the whole variable set (Draper and Smith 1998). It is assumed that the response variable,  $P_{\text{avg}}$ ,  $T_{\text{avg}}$ ,  $T_{\text{min}}$ , or  $T_{\text{max}}$ , is a linear combination of the selected climate indices:

$$y = \beta_0 + \beta_1 x_1 + \beta_2 x_2 + \dots, \quad (1)$$

where  $y$  represents response variable of  $P_{\text{avg}}$ ,  $T_{\text{avg}}$ ,  $T_{\text{min}}$ , or  $T_{\text{max}}$ . The  $x_j$  represents the  $j$ th selected significantly correlated climate index. The  $\beta_j$  is the best-fit regression coefficient of the  $j$ th climate index, and  $\beta_0$  is the intercept term.

The linear regression equations are developed using the data of 1950–90 as the training period and validated with the data of 1990–2015 as validation period (Wang et al. 2015; Li and Wang 2016, 2018; Luo and Wang 2017, 2018; Li et al. 2017; Zhu and Li 2017b). The adjusted coefficients of determination ( $R^2$ ) values are calculated

for estimating the proportion of the variance in the response variables explained by the predictor variables. The formula for adjusted  $R^2$  is as follows:

$$\text{adjusted } R^2 = 1 - \left( \frac{\text{SS}_{\text{resid}}}{\text{SS}_{\text{total}}} \right) \left( \frac{n-1}{n-d-1} \right), \quad (2)$$

where  $\text{SS}_{\text{resid}}$  is the sum of the squared residuals from the regression,  $\text{SS}_{\text{total}}$  is the sum of the squared differences from the mean of the dependent variable (total sum of squares),  $d$  is the total number of predictor variables in the model (not including the constant term), and  $n$  is the sample size. The larger the adjusted  $R^2$  is, the more variability in the response variables is explained by the predictor variables. In addition to adjusted  $R^2$ , the temporal correlation, root-mean-square error (RMSE), and the bias are also calculated to quantify the performance of the linear regression equations.

To explore the atmospheric circulations that are responsible for the connections between  $P_{\text{avg}}$ ,  $T_{\text{avg}}$ ,  $T_{\text{min}}$ , or  $T_{\text{max}}$  and the climate indices, composite analyses of relevant atmospheric variables (i.e., geopotential heights, winds, total cloud coverage, and cloud forcing net longwave and shortwave fluxes at the surface) are conducted in response to different phases of each selected climate index. The atmospheric variables are composited for both positive and negative values of the climate index to represent the circulation patterns for positive and negative phases of the climate index. To ensure the difference in atmospheric variables between the positive and negative phases of the climate index is statistically significant, a two-tailed Student's  $t$  test at the 95% confidence interval is conducted.

A wavelet spectral decomposition technique is used to identify significant signals within the time series of  $P_{\text{avg}}$  and related climate indices (Torrence and Compo 1998; Fierro 2014). A statistical significance test is also performed to assess the robustness of the results. Only a significance level exceeding 95% is considered as statistically significant. The wavelet spectral decomposition is performed using the open source code (downloaded from <http://paos.colorado.edu/research/wavelets/>) hosted by the Department of Atmospheric and Oceanic Sciences at the University of Colorado Boulder.

### 3. Results and discussion

#### a. Long-term trend and extreme events

The first question this paper addresses is how the rainy season average monthly accumulated precipitation, minimum temperature, mean temperature, and maximum temperature, both statewide and over 11 subregions,

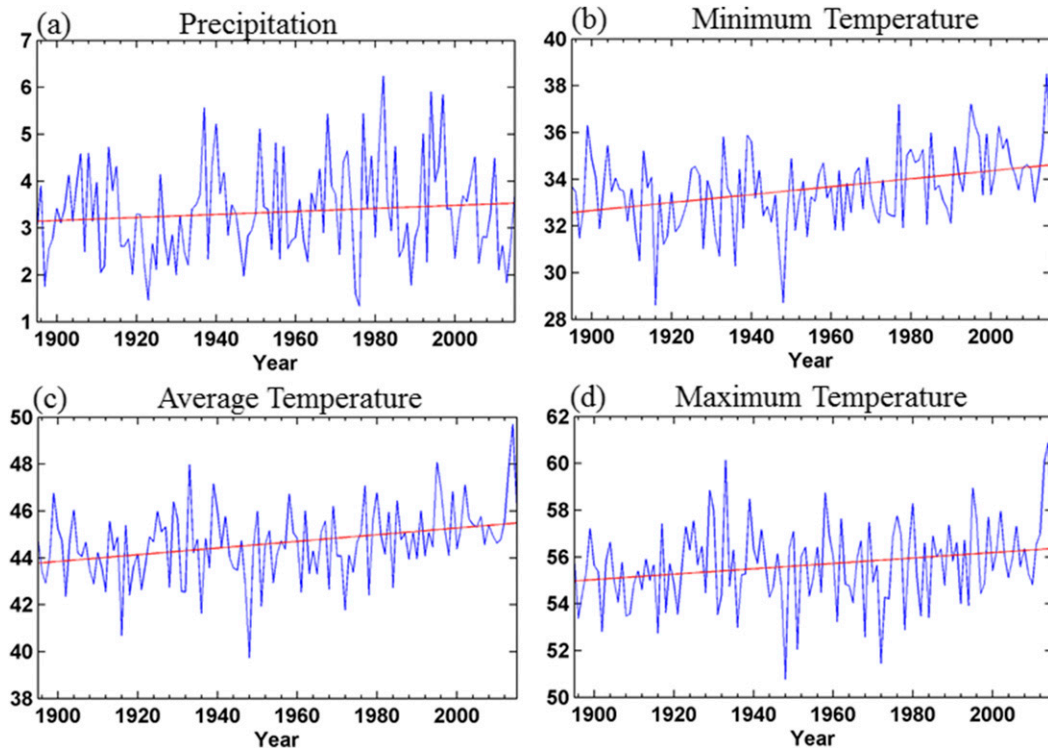


FIG. 2. Time series of statewide (a) rainy season average precipitation (inches), (b) rainy season average minimum temperature ( $^{\circ}\text{F}$ ), (c) rainy season average mean temperature ( $^{\circ}\text{F}$ ), and (d) rainy season average maximum temperature ( $^{\circ}\text{F}$ ) from 1895 to 2015. The red lines are the linear regression line.

have changed during the last century. Hereafter, “rainy season average monthly” will be omitted for the sake of brevity. Figure 2 shows the time series of the statewide accumulated precipitation, minimum temperature, mean temperature, and maximum temperature. The regression slopes, which are indicative of the long-term trends, are presented in Table 2 for the subregions. It can be seen that there is no discernible long-term trend for statewide precipitation over the past 121 years (Fig. 2a). The 11 subregions present a similar long-term trend, except the Sacramento Delta region (E) where the accumulated precipitation has significantly increased with time (Table 2). Although accumulated precipitation has not had a discernible long-term trend from 1895 to 2015, the larger amplitude of accumulated precipitation tends to occur more frequently after 1967 than before 1967. Figure 3 shows that the standard deviations (SD) of accumulated precipitation before 1967 are approximately below 0.95 and have been nearly constant during 1940–67. In contrast, after 1967 the standard deviations increase significantly with time and then become nearly constant during 2000–15. Therefore, 1967 was identified as a turning point for statewide accumulated precipitation. (Fig. 3).

On the other hand, the mean, maximum, and minimum temperatures statewide and for most subregions show a significant warming trend since 1895, except for the Sierra (D), San Joaquin Valley (G), and Sonoran Desert (K) regions for maximum temperature and the North Coast region (A) for minimum temperature (Figs. 2b,c,d for statewide; Table 2 for subregions). Among these three variables, the minimum temperature has the largest warming trend, except for the North Coast (A), North Central (B), and Northeast (C) in which the maximum temperature has the largest warming trend. This suggests a decreased diurnal temperature variation over central and Southern California during the past century (Easterling et al. 1997; Donat et al. 2013), while there is an increased diurnal temperature variation for Northern California. Southern California in general has a larger warming trend than Northern California; in particular, the South Coast region (H) has the highest warming rate for minimum and mean temperatures.

As shown in Fig. 3, larger amplitudes (i.e., standard deviation) in accumulated precipitation have occurred more frequently since 1967. To further investigate this finding, we use a 5-month SPI index to identify different extents of dry and wet scenarios. Figure 4 shows the

TABLE 2. Regression slopes for rainy season average accumulated precipitation (in.), rainy season average minimum temperature ( $^{\circ}\text{F}$ ), rainy season average mean temperature ( $^{\circ}\text{F}$ ), and rainy season average maximum temperature ( $^{\circ}\text{F}$ ) over the 121-yr period for 11 subregions (A–K) and statewide California (CAL). The statistically significant slope is bold.

Regions	Precipitation	Min temp	Mean temp	Max temp
CAL	0.003	<b>0.017</b>	<b>0.014</b>	<b>0.012</b>
A	−0.003	0.005	<b>0.008</b>	<b>0.010</b>
B	0.012	<b>0.012</b>	<b>0.012</b>	<b>0.013</b>
C	0.001	<b>0.013</b>	<b>0.016</b>	<b>0.019</b>
D	0.004	<b>0.019</b>	<b>0.010</b>	0.001
E	<b>0.007</b>	<b>0.018</b>	<b>0.017</b>	<b>0.016</b>
F	0.003	<b>0.018</b>	<b>0.015</b>	<b>0.011</b>
G	0.001	<b>0.020</b>	<b>0.014</b>	0.008
H	0.003	<b>0.026</b>	<b>0.021</b>	<b>0.016</b>
I	−0.001	<b>0.014</b>	<b>0.013</b>	<b>0.013</b>
J	0.001	<b>0.019</b>	<b>0.017</b>	<b>0.015</b>
K	0.001	<b>0.023</b>	<b>0.015</b>	0.007

occurrence rates of extreme wet, moderate wet, normal wet, extreme dry, moderate dry, and normal dry events before and after 1967 for statewide. It is obvious that the occurrences of both extreme dry and wet events and moderate wet events have greatly increased. In contrast, the occurrences of moderate-dry, normal-wet, and normal-dry events have consistently decreased during the same time period. The increased occurrences of extreme dry and wet events can be seen for most of the subregions (see Fig. S2 in SI). This indicates that both intense drought and excessive flooding have increased statewide and for most subregions since 1967, which is consistent with previous studies (Langford et al. 2014;

Herring et al. 2014). This situation is projected to continue in the future based on climate modeling results (Yoon et al. 2015). This may pose a challenge to water management due to higher frequencies of intense drought and excessive flooding events and possible early melting of snowpack resulting from a significant increase in minimum temperatures. Note that because the precipitation and temperature data were obtained from the California Climate Tracker spanning from 1895 to present, it is inevitable that the quality of this dataset can sufferer from smaller number of weather stations available in the early period, especially prior to 1918. To check whether the pre-1918 data have a potential impact on our conclusion, the same analyses are conducted using the data from 1919 to 2015, and almost the same conclusion can be drawn (results not shown). Thus, we may conclude that the data quality prior 1918 does not have a significant impact on our result.

### b. Bootstrapped correlation analysis

To identify the climate indices significantly correlated with and without lags to  $P_{\text{avg}}$ ,  $T_{\text{avg}}$ ,  $T_{\text{min}}$ , and  $T_{\text{max}}$  both statewide and subregionally, a bootstrapped sampling analysis over 1000 random samples of those correlations is conducted. In this analysis, the correlations are considered statistically insignificant if the 2.5% and 97.5% percentiles of the correlation values cross the zero correlation line (Fierro 2014). Figure 5a shows the correlation results between statewide  $P_{\text{avg}}$  and 28 climate indices with different time lags. For climate indices with no lag, the TNH index and the El Niño Modoki C index are the only two climate indices whose 2.5% and 97.5%

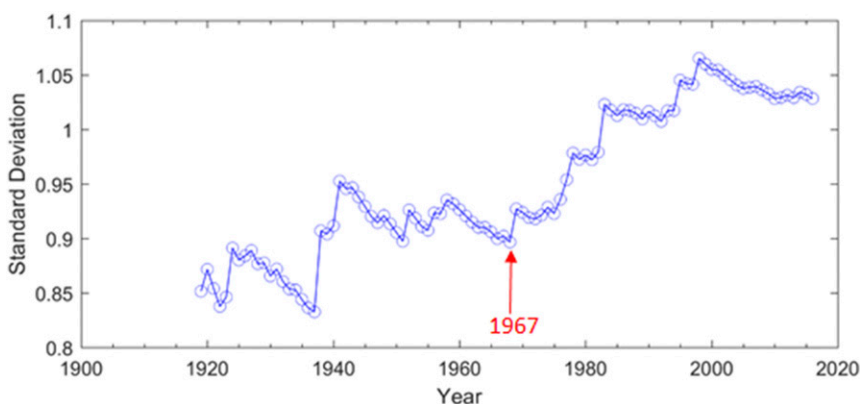


FIG. 3. SD of statewide rainy season average precipitation from 1895 to the year that is indicated by the  $x$  axis. The SD is calculated using the formula  $\sqrt{1/n \sum_{i=1895}^j (X_j - \bar{X})^2}$ , where  $j$  is the given year between 1919 and 2015,  $X_j$  is the statewide rainy season average precipitation from 1895 to the given year  $j$ ,  $\bar{X}$  is the average of statewide rainy season average precipitation from 1895 to the given year  $j$ , and  $n$  is the sample size (the number of years from 1895 to the given year  $j$ ). The red arrow denotes the turning point of 1967.

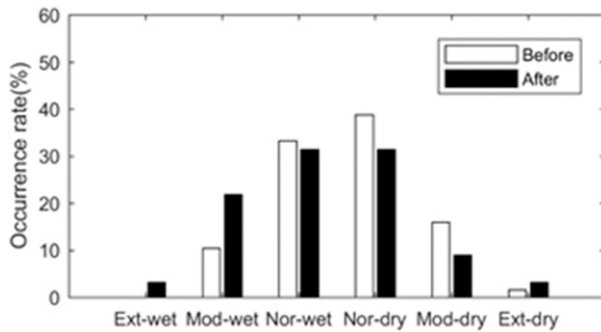


FIG. 4. Occurrence rates (number per month in %) of extreme wet (Ext-wet), moderate wet (Mod-wet), and normal wet (Nor-wet) as well as extreme dry (Ext-dry), moderate dry (Mod-dry), and normal dry (Nor-dry) events based on the 5-month SPI for statewide California for before and after 1967. For the results of subregions please refer to Fig. S2.

percentiles of the correlation coefficients do not cross the zero correlation line, and thus are considered significantly correlated to statewide  $P_{\text{avg}}$ . If multiple time lags for one climate index are found to be significantly correlated to statewide  $P_{\text{avg}}$ , the final time lag for the climate index is determined using the maximum median values of correlation coefficients among different time lags. The same procedure applies to  $T_{\text{avg}}$ ,  $T_{\text{max}}$ , and  $T_{\text{min}}$  statewide and all subregions, and a list of significantly correlated climate indices for  $P_{\text{avg}}$ ,  $T_{\text{avg}}$ ,  $T_{\text{max}}$ , and  $T_{\text{min}}$  statewide and at all the subregions is obtained.

It is shown that the TNH index with no time lag [denoted as TNH(0)] is highly correlated to  $P_{\text{avg}}$  both statewide and for all subregions. The TNH index has the highest correlation with  $P_{\text{avg}}$  in Northern California and the Sierra, and the correlation decreases southward (refer to Figs. S3–S7 in SI for all subregions and time lags). The  $P_{\text{avg}}$  over Northern California (A, B, and C) is significantly correlated to most of the ENSO-related indices 3 to 4 seasons ahead. For example, the El Niño Modoki B (−4) has the median correlations of  $\sim 0.23$  for  $P_{\text{avg}}$  over Northern California. The  $P_{\text{avg}}$  over central and Southern California (F, G, H, I, J, and K) are highly correlated to most of the ENSO-related indices 0 to 2 seasons ahead. Among the ENSO-related indices, the Niño-1+2 (0) and SOI(−1) have the largest correlation magnitudes over the subregions in central California and Southern California, respectively. The longer time lag of the ENSO-related indices for Northern California than for Southern California is expected as Northern California is farther away from the tropics than Southern California. The  $P_{\text{avg}}$  over the North Coast (A), North Central (B), Sierra (D), and the Central California subregions (E and F) is also significantly correlated with the PE index one season ahead. No correlations are found for the TNA, EA, or solar indices to  $P_{\text{avg}}$  in any subregions.

The TNH has been received little attention previously. The above results show that the connection of the TNH(0) index with California precipitation is robust for the long period since 1950. In particular, stronger correlation of the TNH(0) in Northern California than in Southern California is important because there have been no conclusive studies on the dominant climate modes that modulate precipitation variability during the rainy season in Northern California. To further investigate the connections between the TNH(0) index and extreme precipitation (dry or wet) events, the time series of the TNH(0) index and statewide  $P_{\text{avg}}$  are presented in Fig. 6. Please note that the signs of the TNH(0) have been switched in Fig. 6 for a simple comparison. The selection of extreme wet and dry events is based on the top and bottom 15% percentiles of  $P_{\text{avg}}$ , respectively. Figure 6a shows that 1951, 1955, 1968, 1977, 1982, 1985, 1992, 1994, and 1997 were extremely wet years, in which  $P_{\text{avg}}$  correlates well with large positive values of the TNH(0) index in these years, with the exception of 1951. For the extreme dry years, including 1956, 1963, 1975, 1976, 1989, 1993, 2006, 2012, and 2014,  $P_{\text{avg}}$  also correlates well with large negative values of the TNH(0) index with the exception of 1975 in which the TNH(0) index had a very small negative value. Similar results can be obtained from the statewide precipitation averaged over December to February and the TNH(0) index (Fig. 6b), which indicates that correlation between the California precipitation and the TNH(0) index is robust and is not sensitive to the definition of the rainy season.

Different from  $P_{\text{avg}}$ , statewide and most subregional  $T_{\text{min}}$  is highly correlated to the NPI, PDO, PNA, and EPNP indices with no time lag, except for the PNA(0) index in the San Joaquin Valley region (G) (Fig. 5b; refer to Figs. S8–S12 in SI for all subregions and time lags). The  $T_{\text{min}}$  is also significantly correlated to multiple ENSO-related indices 0 to 2 seasons ahead statewide and for many subregions. The correlation magnitudes of  $T_{\text{min}}$  to the PDO, NPI, PNA, and EPNP indices are the highest in the coastal regions and decrease toward inland. No robust correlations are found for  $T_{\text{min}}$  to the El Niño Modoki C, TSA, PE, AO, and QBO indices statewide and for any subregions.

Similar to  $T_{\text{min}}$ ,  $T_{\text{avg}}$  statewide and in most subregions is also found to be significantly correlated to the PDO, NPI, PNA, and EPNP indices with no time lag (Figs. S13–S17), except for the PNA(0) index in the two desert regions (J and K) and the PDO(0) index in the Mojave Desert regions (J). However, the magnitudes of correlation coefficients for those climate indices are smaller than those for  $T_{\text{min}}$ .

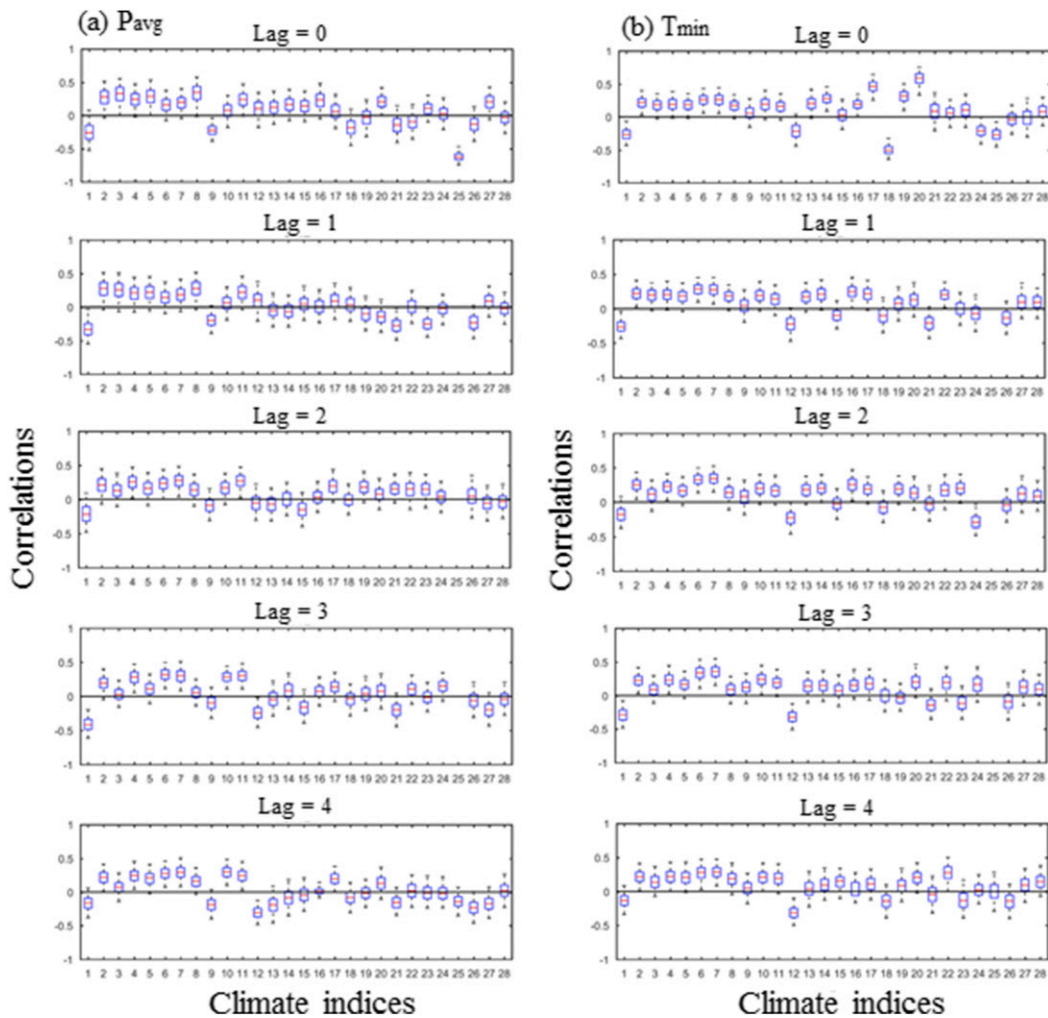


FIG. 5. Box-and-whisker plots of 1000 samples' bootstrapped Pearson's correlation between (a)  $P_{\text{avg}}$  and (b)  $T_{\text{min}}$  and 28 rainy season average climate indices with time lags from 0 to 4 during 1950–2015 for statewide California. The red line within the box depicts the median correlation. The blue box shows the lower and upper quartile (25% and 75%). The 2.5th- and 97.5th-percentile correlation values are shown with the end bars of the dotted lines outside the blue box. The x axis indicates 28 rainy season average climate indices, and the y axis shows the correlation coefficients. For the results of all subregions please refer to Figs. S3–S22.

While  $T_{\text{max}}$  are also significantly correlated with the PDO, NPI, PNA, and EPNP indices with no time lag,  $T_{\text{max}}$  has the lowest median correlation coefficients for those climate indices among the three temperature fields (Figs. S18–S22). In addition,  $T_{\text{max}}$  is significantly correlated with fewer climate indices compared to the other two temperature fields.

Because some of the climate indices are retrieved from SST, they may contain a significant trend during 1950–2015. Since precipitation and temperature fields used in this study are detrended, we would like to ensure that the aforementioned correlation results are robust regardless of whether the climate indices are detrended or nondetrended. We perform a linear regression  $t$  test

with 95% confidence interval to identify which SST-retrieved climate indices have a long-term trend, and six of them are found, including the TNA, TSA, WHWP, Niño-1+2, Niño-4, and El Niño Modoki C indices (results not shown). We detrend these six climate indices and perform the bootstrapped correlation analysis for these detrended climate indices. Results indicate that for  $P_{\text{avg}}$ , except for Niño-1+2(0) and TNA(0), the other four indices have no significant difference in median correlation coefficients between detrended and nondetrended climate indices (results not shown). The median correlation coefficients of detrended Niño-1+2(0) and detrended TNA(0) to  $P_{\text{avg}}$  increase considerably for Northern California and central California compared to

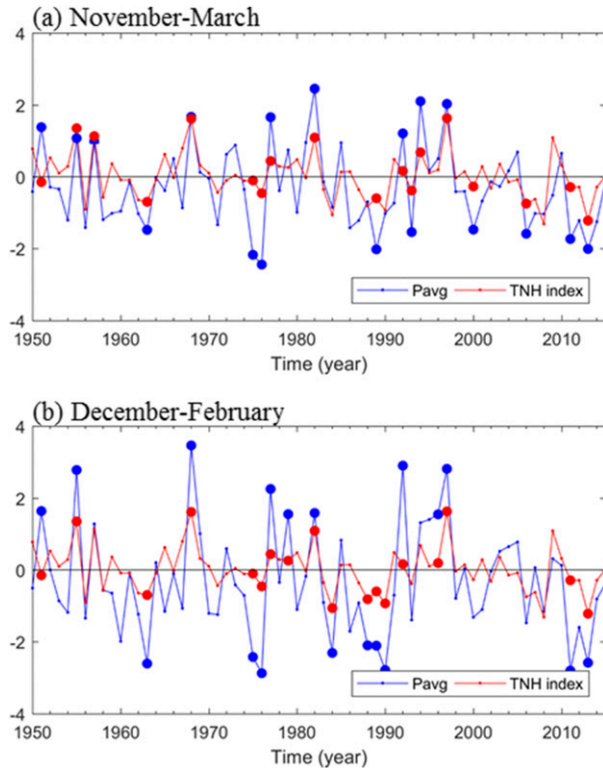


FIG. 6. Time series of the statewide precipitation (blue line) and the TNH index with sign switched (red line) averaged over (a) November to March and (b) December to February. The blue dots indicate the extreme dry and wet events determined using the bottom and top 15th percentile of average precipitation. The red dots indicate the corresponding TNH index values for those extreme events.

nondetrended Niño-1+2(0) and nondetrended TNA(0), respectively. However, even though detrended TNA(0) and detrended Niño-1+2(0) have higher correlation coefficients to  $P_{\text{avg}}$  compared to nondetrended ones, their correlation coefficients are still lower than that of nondetrended TNH(0) for statewide and all the subregions. Similar results can be obtained for  $T_{\text{avg}}$  that all six climate indices have no significant difference in median correlation coefficients between detrended and nondetrended climate indices. Therefore, the conclusion that we obtain from the bootstrapped correlation analysis does not change regardless of whether climate indices are detrended or nondetrended.

### c. Linear regression analysis

Now that we know which climate indices are significantly correlated to  $P_{\text{avg}}$ ,  $T_{\text{min}}$ ,  $T_{\text{max}}$ , and  $T_{\text{avg}}$  in California based on the above analyses, the next step is to examine the predictability of those climate indices for  $P_{\text{avg}}$ ,  $T_{\text{max}}$ ,  $T_{\text{min}}$ , and  $T_{\text{avg}}$ . To accomplish this, we conduct simple linear regression and calculate an associated

adjusted  $R^2$  using the data in the training period (1950–1990). Each significantly correlated climate index obtained from bootstrapped correlation analyses is used as a predictor variable and either  $P_{\text{avg}}$ ,  $T_{\text{max}}$ ,  $T_{\text{min}}$ , or  $T_{\text{avg}}$  is used as a response variable aiming to build the simple linear equations. Note that adjusted  $R^2$  instead of  $R^2$  is used in this study because the former can account for the number of predictor variables in the model. Table 3 shows that for  $P_{\text{avg}}$ , the TNH(0) index has adjusted  $R^2$  of 32% statewide and 14%–31% for all subregions, except for K (refer to Table S2 for completed results). In other words, the TNH(0) index may explain about 32% of  $P_{\text{avg}}$  variation statewide and 14%–31% for the subregions, except for K. In addition, the TNH(0) index has higher adjusted  $R^2$  for Northern California and the Sierra than for Southern California, which suggests the TNH(0) index may have the highest predictability for  $P_{\text{avg}}$  in Northern California and the Sierra, and the predictability of the TNH(0) index for  $P_{\text{avg}}$  would decrease southward. Other indices have much lower adjusted  $R^2$  in Northern and central California compared to the TNH(0) index. This suggests that the TNH(0) pattern may be the most dominant synoptic mode that modulates California precipitation, especially for Northern California and the Sierra. The PE(−1) index has a similar latitude dependence as the TNH(0), although its associated adjusted  $R^2$  is much smaller than that of the TNH(0). In contrast, the SOI(−1) has the highest adjusted  $R^2$  over the southernmost subregions (I, J, and K) and the adjusted  $R^2$  decreases with increasing latitudes, which is consistent with previous studies (Becker et al. 2009; Fierro 2014; Schonher and Nicholson 1989; Mo and Higgins 1998).

For temperature fields of  $T_{\text{min}}$  (Table 3b), the NPI(0) generally has the largest adjusted  $R^2$  values both statewide and for most subregions. The adjusted  $R^2$  values for the PDO(0), EPNP(0), and PNA(0) indices are slightly smaller than that of the NPI(0), but in general they are of comparable magnitudes. In addition, the adjusted  $R^2$  values for the EPNP(0), PDO(0), NPI(0), and PNA(0) indices are the highest at the coastal subregions and decrease toward inland, which is consistent with the results from bootstrapped correlation analysis. Similar results can be obtained for  $T_{\text{max}}$  and  $T_{\text{avg}}$ . Nevertheless, the adjusted  $R^2$  values for  $T_{\text{max}}$  and  $T_{\text{avg}}$  are smaller than that for  $T_{\text{min}}$  (Table S2 in SI).

To further investigate whether any given combinations of the significantly correlated climate indices can improve the predictability for  $P_{\text{avg}}$ ,  $T_{\text{max}}$ ,  $T_{\text{min}}$ , and  $T_{\text{avg}}$ , stepwise multiple linear regression analyses are conducted for  $P_{\text{avg}}$ ,  $T_{\text{max}}$ ,  $T_{\text{min}}$ , and  $T_{\text{avg}}$  statewide and for 11 subregions using the data in the training period (1950–90). Table 4a shows that a combination of significantly

TABLE 3. The adjusted  $R^2$  values (%) of linear regression models between individual climate index and  $P_{\text{avg}}$ ,  $T_{\text{min}}$ ,  $T_{\text{avg}}$ , and  $T_{\text{max}}$  for selected climate indices and subregions during the period of 1950–90 (training period). Please refer to Table S2 in the supporting information for completed results. The number in parentheses indicates the time lags for the climate index with 0 for no time lag,  $-1$  for one season ahead,  $-2$  for two seasons ahead,  $-3$  for three seasons ahead, and  $-4$  for four seasons ahead.

Regions	CAL	North Central (B)	Sierra (D)	Sacramento-Delta (E)	San Joaquin Valley (G)	South Coast (H)
$P_{\text{avg}}$						
SOI( $-1$ )	8	1	2		23	29
PE( $-1$ )	13	16	12		6	1
TNH(0)	32	31	27		26	18
$T_{\text{min}}$						
PDO(0)	12	11		5	6	28
NPI(0)	23	23		14	12	36
PNA(0)	7	8		2	0	21
EPNP(0)	19	11		15	24	35
$T_{\text{avg}}$						
PDO(0)	12	22		9	9	32
NPI(0)	18	26		13	13	33
PNA(0)	11	22		8	6	33
EPNP(0)	8	12		15	17	11
$T_{\text{max}}$						
PDO(0)	6	14		4	4	23
NPI(0)	7	11		3	4	20
PNA(0)	8	17		6	5	30
EPNP(0)	0	4		4	2	0

correlated climate indices improves the predictability of  $P_{\text{avg}}$  for statewide and most of the subregions, except for the Sonoran Desert regions (K) where only the SOI( $-2$ ) index is included as the predictor variable in the equation. The TNH(0) index is included as one of the predictor variables in all multiple regression equations except for the Sonoran region (K). In addition to the TNH(0) index, the PE( $-1$ ) index is also included as another predictor variable for  $P_{\text{avg}}$  in Northern California (A and B), central California (E and F), the Sierra (D), and statewide. For  $P_{\text{avg}}$  in Southern California, in addition to the TNH(0) index, the SOI( $-2$ ) is also included as another predictor in the regression equations. The adjusted  $R^2$  values for the multiple linear regression equations with a combination of the climate indices range from 32% to 60%, which are much higher than those from any single climate index (refer to Table S3 for completed results).

Similar to  $P_{\text{avg}}$ , a combination of the climate indices is suggested as predictor variables in the equations for  $T_{\text{min}}$  statewide and most of the subregions, except for the Sierra (D) where only the NPI(0) is included as a predictor variable in the equation. For the other regions, either the NPI(0), EPNP(0), or PNA(0) indices are often included as one of the predictor variables in the multiple linear regression equations. The adjusted  $R^2$  values of the multiple linear regression equations with a combination of the climate indices range from 27% to

72%, which are much higher than those from any of the single climate index. A similar result can be obtained for  $T_{\text{max}}$  and  $T_{\text{min}}$  (Tables S4–S6 in SI).

While the improved predictability can be obtained from a combination of significantly correlated climate indices, the equations developed in this study are not intended for practical prediction because the ultimate equations that can be used for operational purposes require throughout testing and verification/validation, which is beyond the scope of this paper. The primary purpose of this study is to identify/screen out which climate indices could be potentially used for prediction and to investigate whether a combination of these climate indices can provide a better predictability than a single climate index for precipitation and temperature. Although the CPC of NOAA only uses ENSO as the primary factor to project California's precipitation, our study suggests that the combination of the TNH index and ENSO indices would provide a better prediction for California precipitation than using ENSO indices only.

Note that the above multiple linear regressions are built based on the data of 1950–90 (training period). There is a need to validate whether these equations can still provide reasonable estimates of  $P_{\text{avg}}$ ,  $T_{\text{avg}}$ ,  $T_{\text{max}}$ , and  $T_{\text{min}}$  using other independent data (validation period: 1990–2015). Figure 7a and Table 5a show that the multiple linear regression equations with a combination of the climate indices can provide reasonable estimates of

TABLE 4. Multiple linear regression equations and associated adjusted  $R^2$  values (%) for  $P_{\text{avg}}$ ,  $T_{\text{min}}$ ,  $T_{\text{avg}}$ , and  $T_{\text{max}}$  for selected subregions and statewide California for the period of 1950–90 (training period). Please refer to Tables S3–S6 in the supporting information for completed results. The number in parentheses indicates the time lags for the climate index.

Regions	No. of predictors	Multiple linear equations	Adjusted $R^2$
$P_{\text{avg}}$			
CAL	2	$-0.31 - 0.60 \times \text{PE}(-1) - 0.96 \times \text{TNH}(0)$	40
B	3	$-0.59 + 1.32 \times \text{El Niño Modoki B}(-4) - 1.39 \times \text{PE}(-1) - 2.35 \times \text{TNH}(0)$	52
D	2	$-0.42 - 1.12 \times \text{PE}(-1) - 1.71 \times \text{TNH}(0)$	34
G	2	$-0.25 - 0.04 \times \text{SOI}(-1) - 0.59 \times \text{TNH}(0)$	41
H	3	$-0.20 - 0.06 \times \text{SOI}(-1) + 0.63 \times \text{EPNP}(0) - 0.72 \times \text{TNH}(0)$	45
$T_{\text{min}}$			
CAL	2	$-2.55 - 0.22 \times \text{NPI}(0) + 0.75 \times \text{EPNP}(0)$	32
B	3	$-2.65 + 0.37 \times \text{WHWP}(-2) - 0.78 \times \text{NPI}(0) - 1.94 \times \text{PNA}(0)$	45
E	2	$-3.18 + 0.91 \times \text{EPNP}(0) - 0.86 \times \text{TNH}(0)$	28
G	2	$-3.16 + 1.14 \times \text{EPNP}(0) - 0.93 \times \text{TNH}(0)$	39
H	6	$-4.15 + 0.85 \times \text{MEI}(-2) - 0.65 \times \text{Niño 1 + 2}(-1) - 0.18 \times \text{NPI}(0) + 0.80 \times \text{EPNP}(0) - 0.80 \times \text{WP}(0) + 0.0005 \times \text{Solar}(-4)$	72
$T_{\text{avg}}$			
CAL	2	$-1.91 + 1.80 \times \text{AMO}(-2) - 0.27 \times \text{NPI}(0)$	25
B	2	$-1.68 + 1.72 \times \text{TNA}(-1) - 0.30 \times \text{NPI}(0)$	34
E	1	$-2.47 + 0.92 \times \text{EPNP}(0)$	16
G	1	$-2.00 + 1.01 \times \text{EPNP}(0)$	17
H	4	$-3.47 + 0.90 \times \text{MEI}(-2) - 1.29 \times \text{Niño 1 + 2}(-1) - 0.37 \times \text{NPI}(0) + 0.0008 \times \text{Solar}(-4)$	53
$T_{\text{max}}$			
CAL	3	$-1.40 + 2.78 \times \text{TNA}(-1) + 0.84 \times \text{PNA}(0) - 1.27 \times \text{WP}(0)$	30
B	2	$-0.97 + 1.15 \times \text{PNA}(0) + 0.99 \times \text{PE}(-1)$	25
E	1	$-1.91 + 2.53 \times \text{TNA}(-1)$	8
G	1	$-0.97 + 2.64 \times \text{TNA}(-1)$	7
H	1	$-1.65 + 1.30 \times \text{PNA}(0)$	30

$P_{\text{avg}}$  for the training period of 1950–90 with temporal correlations of 0.59–0.81, RMSE of 0.23–1.98, and bias of  $\sim 0$  for statewide and the subregions (please refer to Table S7 and Fig. S23 for completed results). For the validation period of 1990–2015, reasonable estimates of  $P_{\text{avg}}$  are also obtained with temporal correlation of 0.43–0.68, RMSE of 0.4–2.39, and bias of  $-0.5$ –0.1.

For  $T_{\text{min}}$ , the multiple linear regression equations with a combination of the climate indices can also reproduce the observed  $T_{\text{min}}$  for 1950–90 with temporal correlations of 0.55–0.87, RMSE of 0.87–1.45, and bias of  $\sim 0$  for statewide and subregions (Fig. 7b, Table S7, and Fig. S24). The estimates of  $T_{\text{min}}$  for the validation period of 1990–2015 are also reasonably provided. The only exception is for the Sierra (D) where the temporal correlation is 0.37, which is statistically insignificant.

In addition, the multiple linear equations with the combined climate indices can provide reasonable estimates of  $T_{\text{max}}$  for the training period at some of the subregions (Table 5, Table S7, and Fig. S26). Nevertheless, they have low predictability for  $T_{\text{max}}$  for many subregions during the validation period. Similar results can also be obtained for  $T_{\text{avg}}$  over the statewide,

Northern Central (B), Sierra (D), and South Coast (H) regions.

To investigate whether the low predictability for  $T_{\text{max}}$  and  $T_{\text{avg}}$  during the validation period is caused by the long-term trend inherited from the SST-retrieved climate indices, such as TNA and TSA. We detrend the six climate indices from 1950 to 2015 and use the same procedure to generate the multiple linear regressions with a combination of the climate indices. Similar low predictability of  $T_{\text{max}}$  and  $T_{\text{avg}}$  during the validation period is obtained (results not shown). This suggests that the low predictability of  $T_{\text{max}}$  and  $T_{\text{avg}}$  is not caused by whether the climate indices are detrended or nondetrended.

In fact, compared to  $T_{\text{min}}$ , the much lower predictability for  $T_{\text{max}}$  and  $T_{\text{avg}}$  is not surprising because the median correlation coefficients and adjusted  $R^2$  values for each climate index are much lower than those for  $T_{\text{min}}$ . There are two possible reasons for the low predictability of  $T_{\text{max}}$  and  $T_{\text{avg}}$ . First, the relationships of  $T_{\text{avg}}$  and  $T_{\text{max}}$  to the climate indices might not be linear; they could be nonlinear, which does not satisfy the assumption that we used for our linear regression analysis.

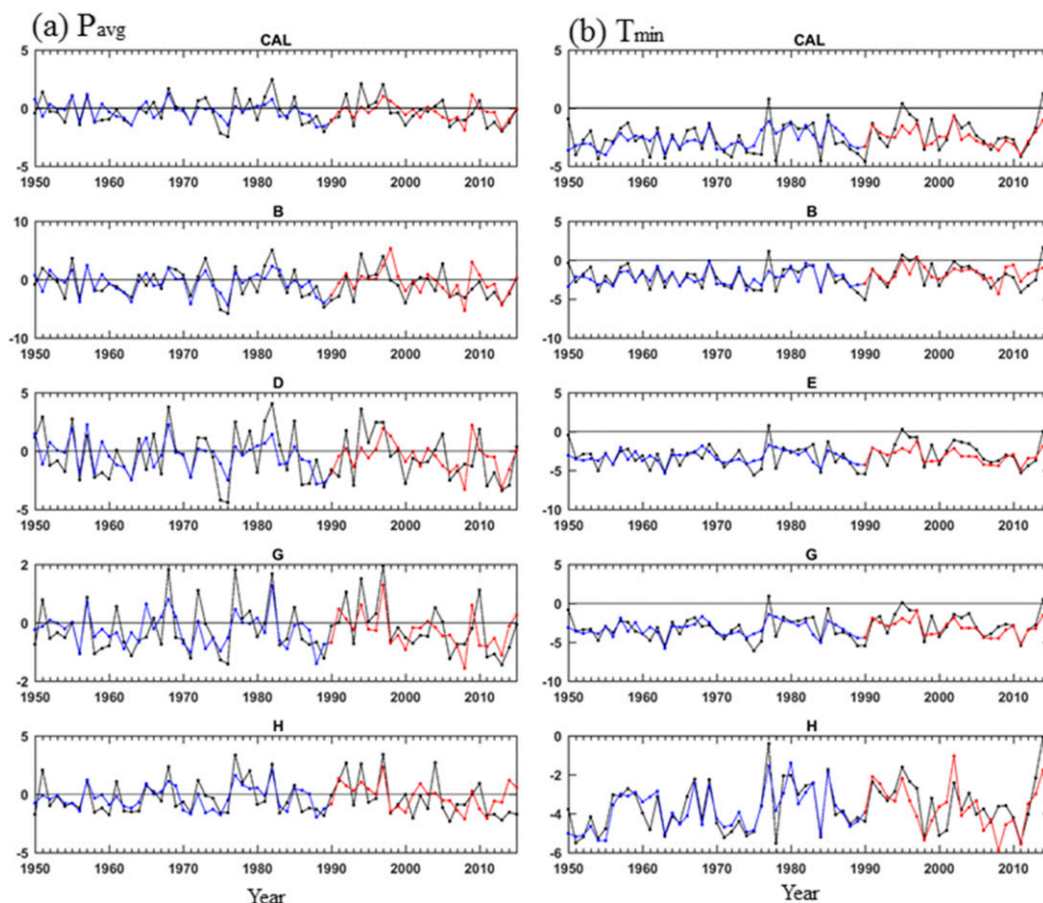


FIG. 7. The time series of the observed (black line) and estimate (blue line for the training period; red line for the validation period) (a)  $P_{\text{avg}}$  and (b)  $T_{\text{min}}$  for statewide and selected subregions. Please refer to Figs. S23–S26 for completed results.

Second, the key or the dominate climate indices related to  $T_{\text{max}}$  and  $T_{\text{avg}}$  might not be included in these 28 climate indices. Further study is required to find the key climate indices for  $T_{\text{max}}$  and  $T_{\text{avg}}$ , and they are outside the scope of this study.

*d. Atmospheric processes for linkages between climate indices and California temperature/precipitation*

To understand how the TNH(0) pattern influences precipitation over California, we perform a composite analysis of various rainy season average detrended atmospheric variable anomalies for positive and negative TNH(0) index phases. Hereafter, “rainy season average detrended” will be omitted for the sake of brevity. The composites of rainy season average long-term means (1981–2010) for 500- and 950-hPa geopotential heights and winds, 950-hPa water vapor mixing ratio, and total cloud fraction are presented in Fig. 8 for a reference. The composites of geopotential height anomalies in

Fig. 9a show a deep, east–west dipole comprising a strong positive height anomaly, accompanied by an anticyclonic circulation anomaly, anchored to the northwest of California, and a strong negative height anomaly, accompanied by a cyclonic circulation anomaly, sitting over eastern Canada during positive TNH(0) index. The strong positive height anomaly strengthens the climatological mean ridge (Fig. 8a), which reduces the likelihood of winter storms reaching and affecting California, and deflects them toward the north and south (Wang et al. 2014; Chang et al. 2015). This can be seen in the composite of total cloud fraction anomaly in which large positive cloud fraction anomalies are located over western Canada and Mexico, while negative water vapor mixing ratio and total cloud fraction anomalies are located over California (Figs. 9d,g). In addition, the wind anomalies associated with height anomalies extend from the middle levels down to the low levels (Fig. 9g). The low-level northerly wind anomalies between the dipole of height anomalies advect more dry air from higher

TABLE 5. The adjusted  $R^2$  (%), temporal correlation (CC), RMSE, and bias between the observed and estimated  $P_{\text{avg}}$ ,  $T_{\text{min}}$ ,  $T_{\text{avg}}$ , and  $T_{\text{max}}$  obtained using data during 1950–90 (training period) and during 1990–2015 (validation period) for statewide and selected subregions. Please refer to Table S7 in the supporting information for completed results. The statistically significant CC is bolded.

Regions	$R^2$ (training)	$R^2$ (validation)	CC (training)	CC (validation)	RMSE (training)	RMSE (validation)	Bias (training)	Bias (validation)
$P_{\text{avg}}$								
CAL	40	45	<b>0.65</b>	<b>0.58</b>	0.84	0.88	0.00	−0.01
B	52	47	<b>0.74</b>	<b>0.54</b>	1.66	2.22	0.00	−0.50
D	34	28	<b>0.61</b>	<b>0.51</b>	1.70	1.68	0.00	−0.07
G	41	44	<b>0.66</b>	<b>0.62</b>	0.62	0.67	0.00	0.10
H	45	26	<b>0.70</b>	<b>0.50</b>	0.97	1.44	0.00	−0.15
$T_{\text{min}}$								
CAL	32	55	<b>0.60</b>	<b>0.76</b>	1.02	0.98	0.00	0.35
B	45	37	<b>0.70</b>	<b>0.60</b>	1.00	1.25	0.00	−0.09
E	28	59	<b>0.56</b>	<b>0.79</b>	1.16	1.15	0.00	0.50
G	39	62	<b>0.65</b>	<b>0.81</b>	1.08	1.09	0.00	0.55
H	72	64	<b>0.87</b>	<b>0.68</b>	0.59	0.97	0.00	0.24
$T_{\text{avg}}$								
CAL	25	3	<b>0.53</b>	0.32	1.11	1.26	0.00	0.11
B	34	10	<b>0.61</b>	0.38	1.02	1.34	0.00	−0.21
E	16	45	<b>0.42</b>	<b>0.68</b>	1.13	1.13	0.00	0.57
G	17	46	<b>0.44</b>	<b>0.70</b>	1.17	1.14	0.00	0.64
H	53	−4.3	<b>0.76</b>	0.06	0.84	1.58	0.00	0.33
$T_{\text{max}}$								
CAL	30	15	<b>0.60</b>	0.37	1.37	1.61	0.00	−0.41
B	25	10	<b>0.54</b>	0.22	1.53	1.96	0.00	0.29
E	8	0	0.31	0.19	1.64	1.75	0.00	−0.04
G	7	−1	0.31	0.17	1.74	1.75	0.00	0.01
H	30	−4	<b>0.56</b>	0.02	1.37	1.55	0.00	−0.07

latitudes to California, further discouraging the formation of clouds and precipitation (Fig. 9g). In contrast, during negative TNH(0) index, a strong negative height anomaly, accompanied by a cyclonic circulation anomaly, is centered over the Gulf of Alaska, and another negative height anomaly is located from the Gulf of Mexico northeastward across the western North Atlantic (Fig. 9b). Furthermore, a strong positive height anomaly is located around Hudson Bay throughout eastern Canada. This synoptic pattern favorably steers winter storms across the western United States, which brings in large positive cloud and precipitation anomalies, in particular, to Northern California, Oregon, and Washington (Fig. 9e), where the 500-hPa southwesterly wind anomaly reaches a maximum near the West Coast (Fig. 9b). In addition, the low-level southerly wind anomalies counteract the northwesterly winds associated with the climatological mean ridge (Figs. 9h and 8b), which advects less dry air from higher latitudes southward and more moist air from the Pacific Ocean into the western United States, promoting the formation of clouds and precipitation. It is worth mentioning that the water vapor and total cloud fraction anomalies are also more pronounced in Northern California than

Southern California during the negative TNH(0) phase. This might explain why the TNH(0) index is better correlated to the variability of  $P_{\text{avg}}$  in Northern California than in Southern California. The aforementioned differences between positive and negative TNH(0) phases are all statistically significant as shown in Figs. 9e,f,i.

Temperature fields, including  $T_{\text{avg}}$ ,  $T_{\text{max}}$ , and  $T_{\text{min}}$ , can be modulated by the atmospheric modes in two ways. First, the wind effect: the modes can modulate geopotential heights and associated wind fields to transport either warmer air from lower latitudes or colder air from higher latitudes to local areas (Myoung et al. 2015; Bond et al. 2015). Second, the cloud radiation effect: the modes can modulate the cloud formation, which affects Earth’s radiation balance via the cloud albedo and cloud greenhouse forcings (Rossow and Lacis 1990; Rossow and Zhang 1995; Zhu and Li 2017a). The contributions of these two effects to temperature fields can either be counteracted or reinforced depending on the synoptic environment. The analyses here focus on the low-level geopotential heights and winds, as well as total cloud fraction and net cloud forcing that are associated with the NPI(0). Figure 10 shows that during

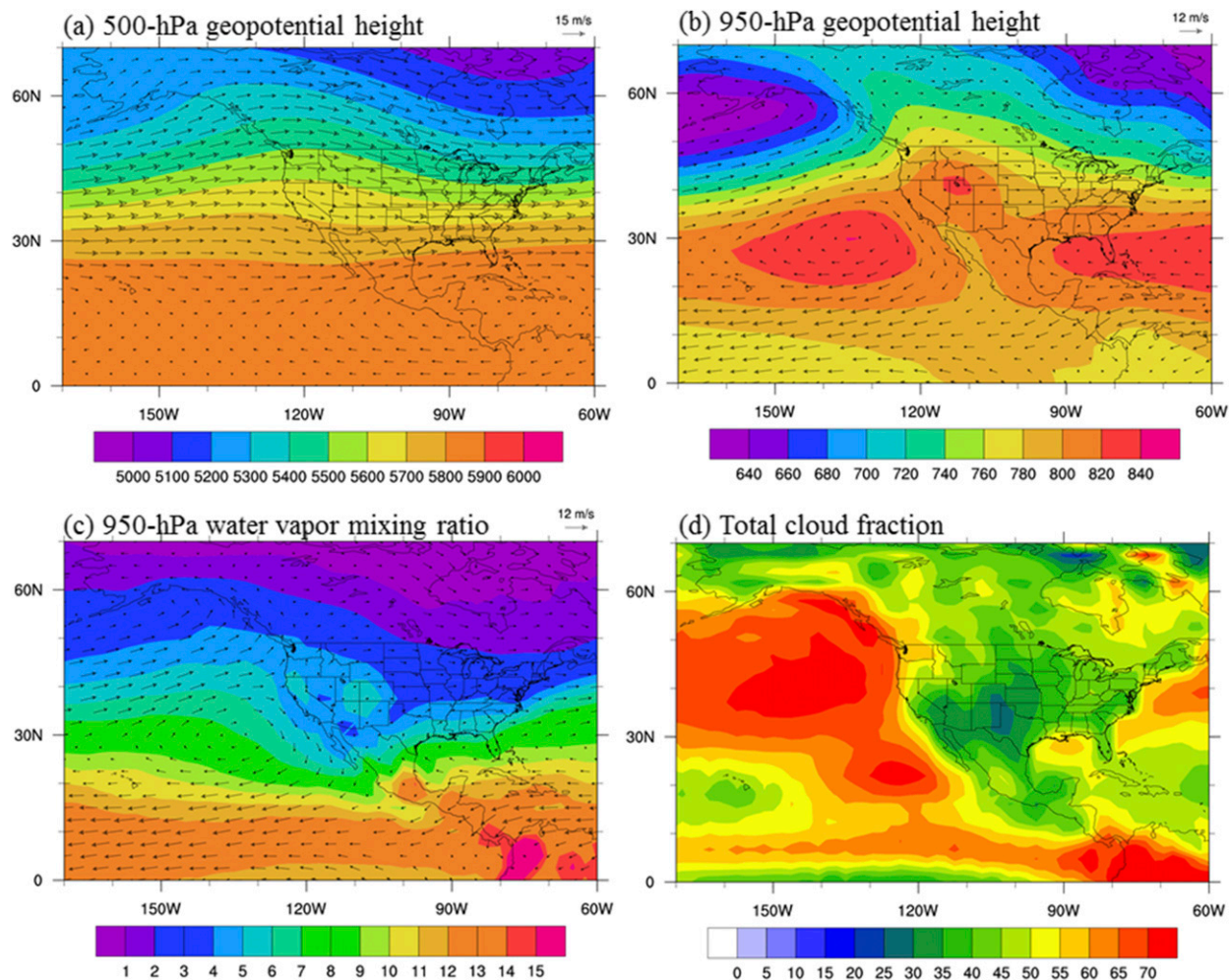


FIG. 8. The composite of rainy season average long-term mean for (a) 500-hPa geopotential height (shading; m) and winds (wind arrows;  $\text{m s}^{-1}$ ), (b) 950-hPa geopotential height (shading; m) and winds (wind arrows,  $\text{m s}^{-1}$ ), (c) 950-hPa water vapor mixing ratio (shading;  $\text{g kg}^{-1}$ ) and wind (wind arrows), and (d) total cloud fraction (%).

negative NPI(0), a similar synoptic pattern is observed, which comprises a negative height anomaly positioned over the northeastern Pacific Ocean. The cyclonic circulation anomalies associated with the negative height anomaly weaken the anticyclonic circulation associated with the climatological mean ridge, which reduces the cold advection from higher latitudes to California, resulting in increased temperature fields (i.e.,  $T_{\min}$ ) at low levels in California. In contrast, during positive NPI(0), a strong positive height anomaly anchors over the northeastern Pacific Ocean, inducing anomalous northwesterly winds around California. The northwesterly wind transports cold air into the region, reducing low-level temperature fields. This might also explain the different influence of the NPI(0) patterns on temperature fields between the coastal areas and the inland areas, because the cold/warm advection has the maximum

impacts on the coastal regions, and the impact decreases when advection is farther inland in California owing to surface friction.

For cloud radiation effects, the NPI(0) modes exhibit statistically significant differences in total cloud fraction anomalies between positive and negative phases (Figs. 10d,e,f). However, their associated net cloud forcings show no statistically significant differences between positive and negative phases (figures not shown). This suggests that the cloud radiation effects associated with the NPI(0) on California surface temperature fields would not be significant. Similar mechanisms can be applied for the other three important climate indices, the EPNP(0), NPI(0), and PNA(0) indices (Figs. S27 and S28 in the SI). We may conclude that the EPNP(0), PNA(0), NPI(0), and PDO(0) patterns modulate the temperature fields, in particular  $T_{\min}$ , via changes to

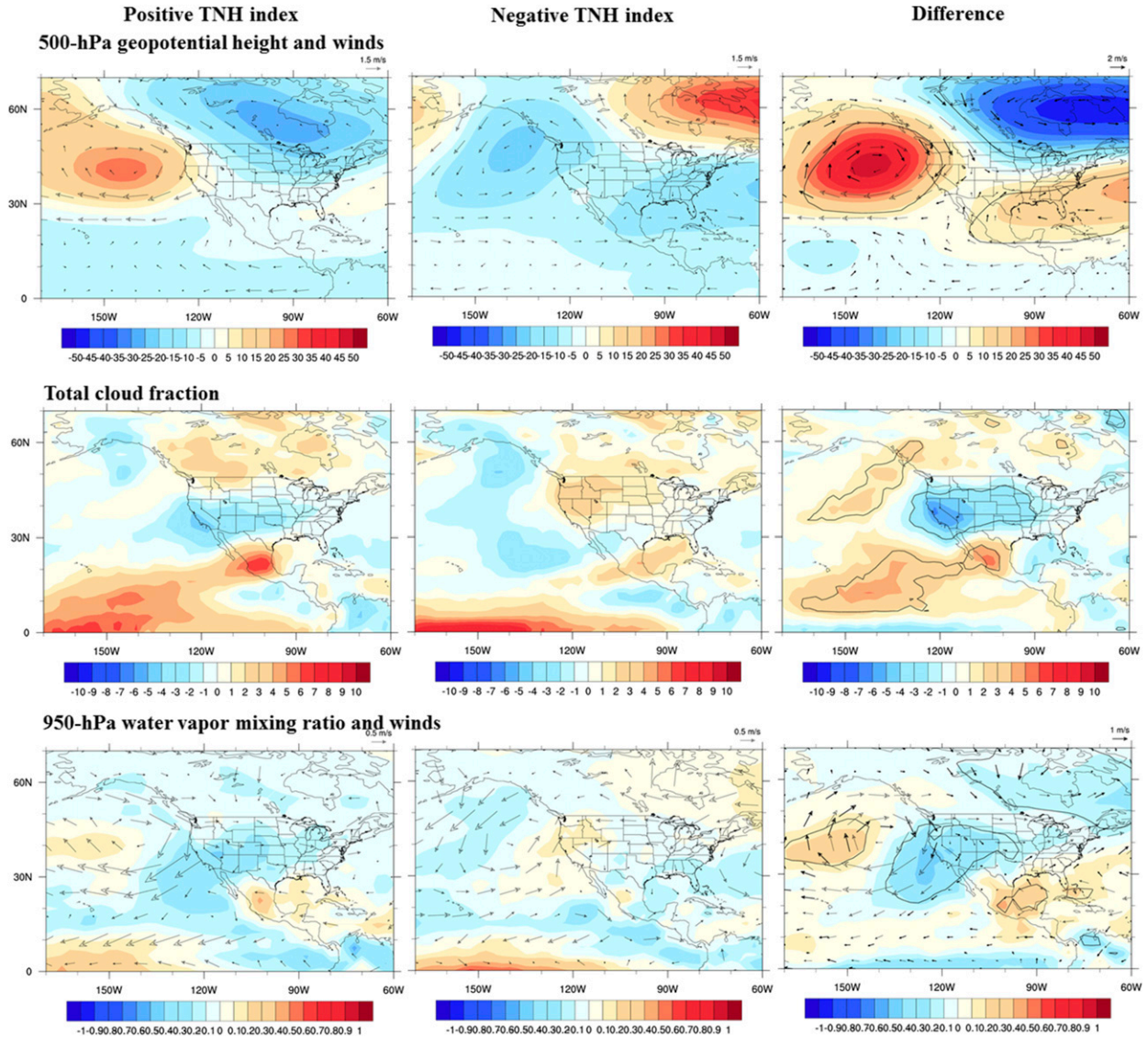


FIG. 9. The composite of rainy season average detrended (a)–(c) 500-hPa geopotential height anomalies (shading; m) and wind anomalies (wind arrows), (d)–(f) total cloud fraction anomalies (%), and (g)–(i) 950-hPa water vapor mixing ratio anomalies (shading;  $\text{g kg}^{-1}$ ) and wind anomalies (wind arrows) for (left columns) the positive TNH index and (center columns) the negative TNH index. (right column) The differences in composite between the positive and negative TNH index. The thick black contours represent the 95% confidence level for the shaded fields, and the bolded wind vectors represent the 95% confidence level for the wind difference.

low-tropospheric wind directions and associated warm/cold advections rather than via changes to cloud radiation effects.

#### e. Wavelet spectral decomposition

To identify significant signals within the time series of  $P_{\text{avg}}$ , wavelet power spectra are computed for  $P_{\text{avg}}$  spanning the period of 1895–2015. Figure 11 shows that during the time period of 1940–67, there were several short time periods with strong 2–4- and 4–8-yr as well as 10–16-yr signals for Northern and central California

(A, B, C, D, E, and F), but no significant signals for Southern California (G, H, I, J, and K; see Fig. S29 for all subregions). Since 1967, the occurrence of strong 2–8-yr signals has become more frequent, particularly since 1980 in Southern California. In addition, the strong 10–16-yr signals have continued to appear for approximately 40 years for most subregions in Northern and central California and for about 30 years in the subregions of Southern California (G, H, U, J, and K). Note that the power values are only statistically significant outside the cone of influence and are

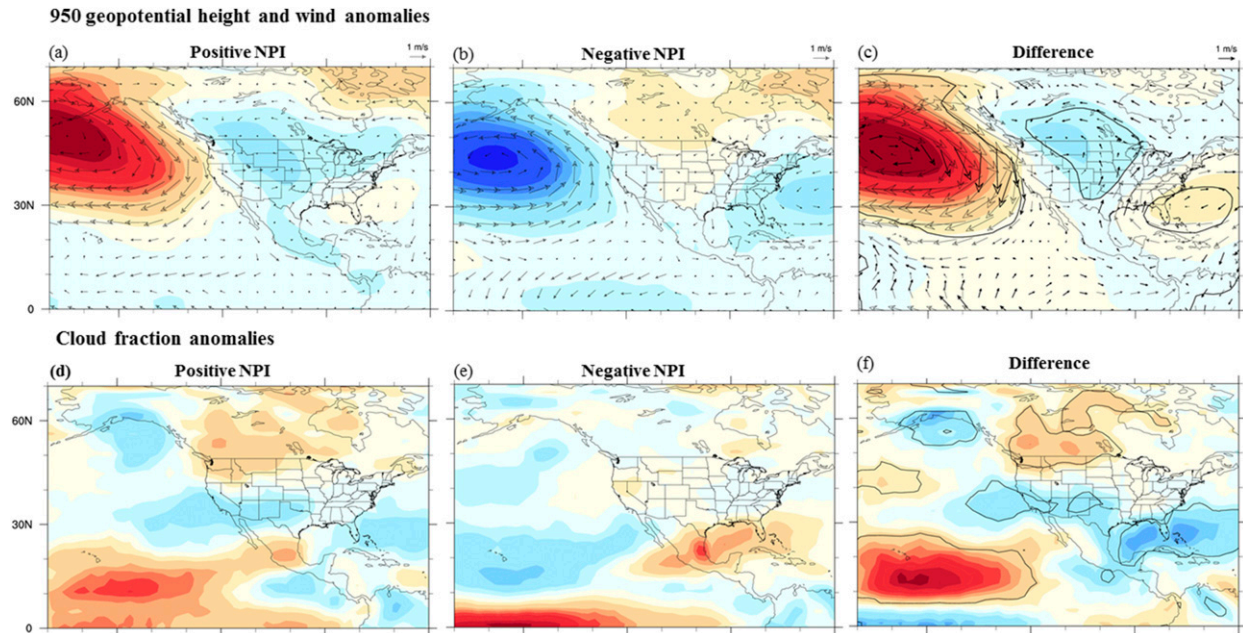


FIG. 10. The composite of rainy season average detrended (a)–(c) 950-hPa geopotential height anomalies (shading; m) and wind anomalies (wind arrows) and (d)–(f) total cloud fraction anomalies (%) for the (left) positive NPI, (center) negative NPI, and (right) their difference. The thick black lines represent the 95% confidence level for the shaded fields, and the black bolded wind vectors represent the 95% confidence level for the wind difference. For the results of the EPNP, PDO, and PNA indices, please refer to Figs. S27 and S28.

highlighted by the 95% confidence interval (thick black contours).

We also apply the wavelet spectral technique to decompose the climate indices that are important to  $P_{\text{avg}}$ , including the TNH(0), MEI(0), Niño-3.4(0), and Niño-1+2(0) indices (Fig. 12). Note that for the climate indices, the wavelet spectral decomposition is conducted for the period of 1950 to 2015 due to limited data availability. It is shown that the TNH index has strong 10–16-yr signals during 1960–91 and strong 2–3-yr signals during 1955–58 (Fig. 12a). Both the MEI and Niño-3.4 indices have a very similar pattern with strong 2–4- and 4–6-yr signals during 1967–72, 1982–90, and 1995–2000 (Figs. 12b,c), which is consistent with the results from Torrence and Compo (1998). The Niño-1+2 index has strong 2–8-yr signals, which occurred at the same time as the MEI and the Niño-3.4 (Fig. 12d).

#### 4. Concluding remarks

To better understand the change in California's climate over the past century, the long-term climate variability and extreme events of precipitation as well as minimum, mean, and maximum temperatures during the rainy season are investigated. The rainy season is defined as November to March in this study. Their relationships to 28 rainy season average climate indices

with and without time lags are also studied. The analyses are based on the observational data from 1895 to 2015, which are in the form of rainy season average detrended monthly accumulated precipitation anomalies  $P_{\text{avg}}$ , averaged detrended monthly maximum temperature anomalies  $T_{\text{max}}$ , averaged detrended monthly mean temperature anomalies  $T_{\text{avg}}$ , and averaged detrended monthly minimum temperature anomalies  $T_{\text{min}}$  both statewide and for 11 geographical subregions. All of 28 climate indices are monthly data initially and are averaged from November to March to become rainy season average climate indices. Hereafter, "rainy season average" for climate indices will be omitted for the sake of brevity.

The present study shows that  $P_{\text{avg}}$  for most of the subregions and the entire state is highly correlated with the TNH index at zero time lag. The TNH(0) index has the highest correlation with  $P_{\text{avg}}$  in Northern California and the Sierra, and the correlation decreases southward. This suggests that the TNH(0) index could be a very useful index for predicting the trend of  $P_{\text{avg}}$  and extreme events in California, especially in Northern California and the Sierra. This is a valuable finding because there have been no conclusive studies on the dominant climate modes that modulate precipitation variability during the rainy season in Northern California.

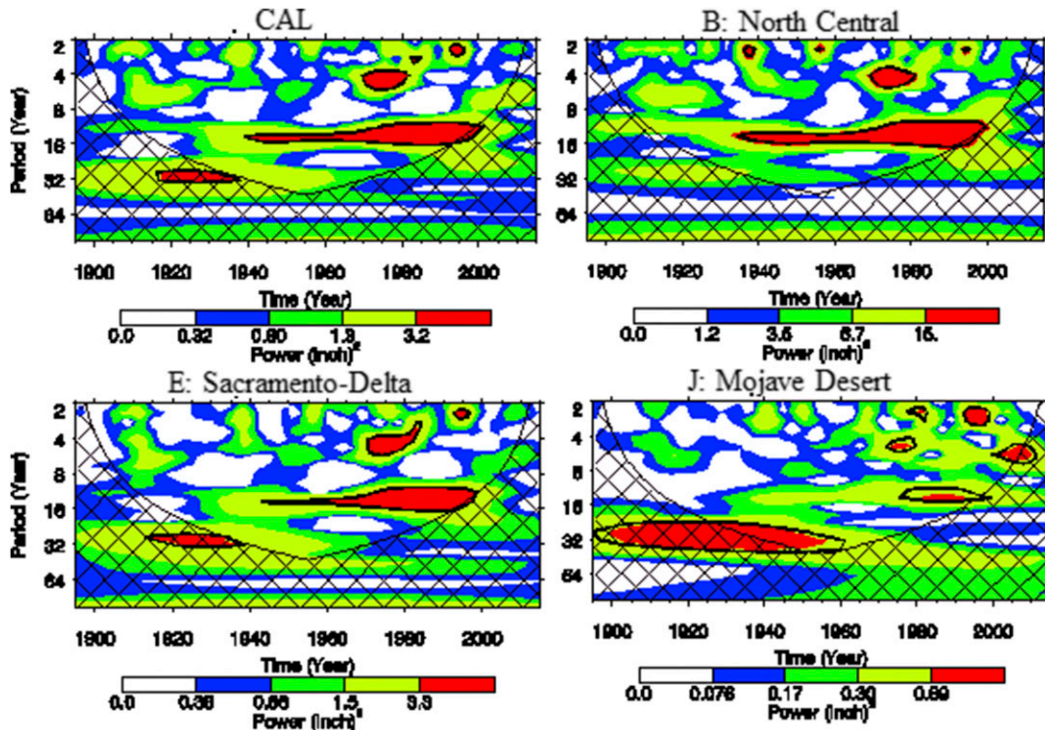


FIG. 11. The wavelet power spectrum of  $P_{\text{avg}}$  for statewide California (CAL) and selected subregions with  $x$  axis indicating time and  $y$  axis indicating period. The contour levels are chosen so that 75%, 50%, 25%, and 5% of the wavelet powers are above their corresponding levels. Therefore, the color bars are different for different subregions. The cross-hatched region is the cone of influence, where zero padding has reduced the variance. The black contour is the 5% significance level, using a white-noise background spectrum. For the results of all subregions, please refer to Fig. S29.

The high correlation between the TNH(0) pattern and  $P_{\text{avg}}$  can be attributed to the development of a strong positive height anomaly and negative height anomaly over the northeast Pacific Ocean at positive and negative TNH(0) phases, respectively. The strong positive height anomaly during positive TNH(0) phase strengthens the climatological mean ridge, which reduces the likelihood of winter storms reaching and affecting California. The northerly wind anomalies associated with the positive height anomaly advect more dry air from higher latitudes to California. Both conditions are unfavorable for cloud formation and precipitation, causing decreased precipitation in California. In contrast, the negative height anomaly at negative TNH(0) phase encourages winter storms to move across the western United States, and their associated southerly wind anomalies to transport less dry air from higher latitudes and more moist air from the Pacific Ocean to California. These conditions are favorable for cloud formation and precipitation, resulting in increased precipitation.

In addition to the TNH(0) index,  $P_{\text{avg}}$  over central California and Southern California is also highly related to ENSO, which is represented by the Niño-1+2(0)

indices and the SOI(-1). Their correlations increase with decreasing latitudes, which is consistent with previous studies.

Temperature fields, in particular  $T_{\text{min}}$ , for 11 geographic subregions and statewide are primarily modulated by the EPNP, PDO, PNA, and NPI patterns at zero time lag. All of the patterns have the largest influence on temperature fields in the coastal regions, and the influence decreases inland. The EPNP(0), PDO(0), PNA(0), and NPI(0) patterns modulate the temperature fields ( $T_{\text{avg}}$ ,  $T_{\text{max}}$ , and  $T_{\text{min}}$ ) via the wind effect. In positive EPNP(0), negative NPI(0), positive PDO(0), or positive PNA(0) phases, the low-level cyclonic wind anomalies transport more warm air from lower latitudes and less cold air from higher latitudes into California, resulting in increased surface temperatures. In contrast, in negative EPNP(0), positive NPI(0), negative PDO(0), or negative PNA(0) phases, an opposite process (i.e., low-level anticyclonic wind anomalies transporting more cold air from higher latitudes into California) results in decreased surface temperatures.

The results presented in this study show that for each subregion and statewide,  $P_{\text{avg}}$ ,  $T_{\text{max}}$ ,  $T_{\text{avg}}$ , and  $T_{\text{min}}$  are

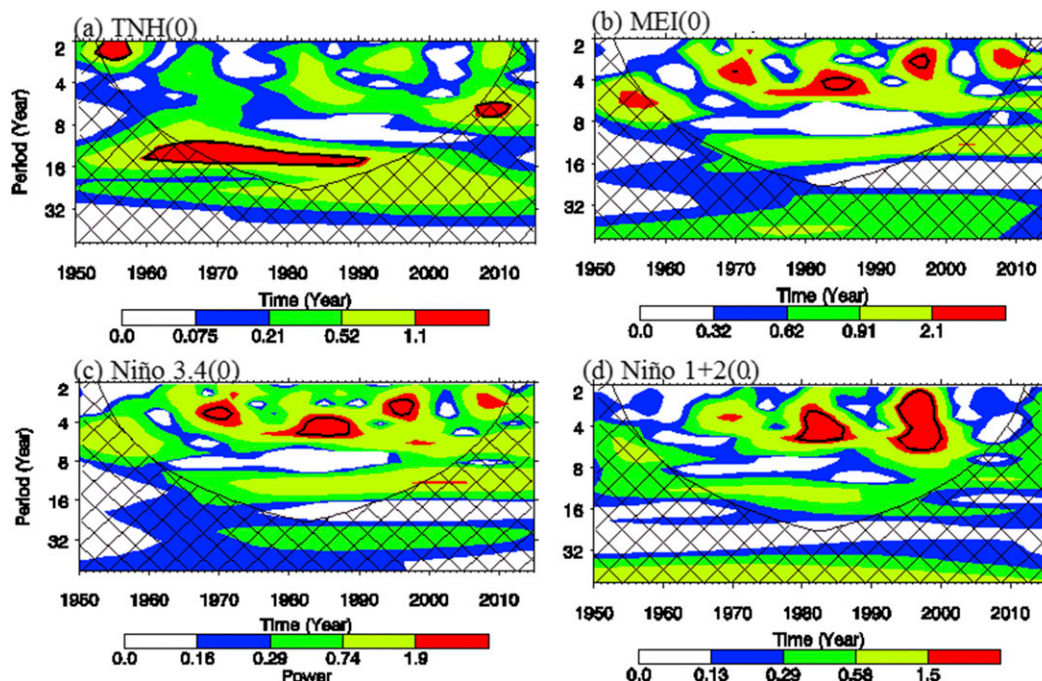


FIG. 12. As in Fig. 11, but for the climate indices (a) TNH(0), (b) MEI(0), (c) Niño-3.4(0), and (d) Niño-1+2(0).

modulated by multiple climate indices. The regression analyses suggest that a combination of important climate indices would improve the predictability of precipitation and minimum temperature statewide and for most of the subregions compared to the use of a single climate index. Nevertheless, the predictability of maximum and mean temperatures is relatively low regardless of using a single or a combination of the climate indices.

Long-term trend analysis shows that rainy season average accumulated precipitation does not have a discernible long-term trend over the past 121 years (1895–2015), but the occurrences of extreme dry and wet events have increased considerably since 1967. In contrast, the rainy season average temperature fields show a significant warming trend since 1895 with different warming rates in minimum and maximum temperatures, resulting in a decreased diurnal variation over central and Southern and an increased diurnal variation over Northern California. In addition, Southern California in general has a larger warming rate than Northern California does; in particular, the South Coast region (H) has the highest warming rate.

*Acknowledgments.* Professor Shu-Hua Chen was supported by NSF Grant 1321720 and NASA Grant NNX16AP17G S01. The authors thank Dr. Xue-meng Chen from CARB for valuable discussion.

#### REFERENCES

- Abatzoglou, J. T., K. T. Redmond, and L. M. Edwards, 2009: Classification of regional climate variability in the state of California. *J. Appl. Meteor. Climatol.*, **48**, 1527–1541, <https://doi.org/10.1175/2009JAMC2062.1>.
- Ashok, K., H. Nakamura, and T. Yamagata, 2007: Impacts of ENSO and Indian Ocean dipole events on the Southern Hemisphere storm-track activity during austral winter. *J. Climate*, **20**, 3147–3163, <https://doi.org/10.1175/JCLI4155.1>.
- Baldwin, M. P., and Coauthors, 2001: The quasi-biennial oscillation. *Rev. Geophys.*, **39**, 179–229, <https://doi.org/10.1029/1999RG000073>.
- Barnston, A. G., and R. E. Livezey, 1987: Classification, seasonality and persistence of low-frequency atmospheric circulation patterns. *Mon. Wea. Rev.*, **115**, 1083–1126, [https://doi.org/10.1175/1520-0493\(1987\)115<1083:CSAPOL>2.0.CO;2](https://doi.org/10.1175/1520-0493(1987)115<1083:CSAPOL>2.0.CO;2).
- Becker, E. J., E. H. Berbery, and R. W. Higgins, 2009: Understanding the characteristics of daily precipitation over the United States using the North American Regional Reanalysis. *J. Climate*, **22**, 6268–6286, <https://doi.org/10.1175/2009JCLI2838.1>.
- Bond, N. E., M. F. Cronin, H. Freeland, and N. Mantua, 2015: Causes and impacts of the 2014 warm anomaly in the NE Pacific. *Geophys. Res. Lett.*, **42**, 3414–3420, <https://doi.org/10.1002/2015GL063306>.
- Carrillo, C. M., C. L. Castro, H.-I. Chang, and T. M. Luong, 2017: Multi-year climate variability in the southwestern United States within a context of a dynamically downscaled twentieth century reanalysis. *Climate Dyn.*, **49**, 4217–4236, <https://doi.org/10.1007/s00382-017-3569-1>.
- Cayan, D. R., and K. T. Redmond, 1994: ENSO influences on atmospheric circulation and precipitation in the western United States. *Proc. 10th Annual Pacific Climate (PACLIM)*

- Workshop*, Pacific Grove, CA, California Department of Water Resources, 5–26.
- Chang, E. K. M., C. Zheng, P. Lanigan, A. M. W. Yau, and J. D. Neelin, 2015: Significant modulation of variability and projected change in California winter precipitation by extratropical cyclone activity. *Geophys. Res. Lett.*, **42**, 5983–5991, <https://doi.org/10.1002/2015GL064424>.
- Donat, M. G., and Coauthors, 2013: Updated analyses of temperature and precipitation extreme indices since the beginning of the twentieth century: The HadEX2 dataset. *J. Geophys. Res. Atmos.*, **118**, 2098–2118, <https://doi.org/10.1002/jgrd.50150>.
- Draper, N. R., and H. Smith, 1998: *Applied Regression Analysis*. Wiley-Interscience, 736 pp.
- Easterling, D. R., and Coauthors, 1997: Maximum and minimum temperature trends for the globe. *Science*, **277**, 364–367, <https://doi.org/10.1126/science.277.5324.364>.
- Enfield, D. B., A. M. Mestas-Núñez, D. A. Mayer, and L. Cid-Serrano, 1999: How ubiquitous is the dipole relationship in tropical Atlantic sea surface temperatures? *J. Geophys. Res.*, **104**, 7841–7848, <https://doi.org/10.1029/1998JC900109>.
- , —, and P. J. Trimble, 2001: The Atlantic multidecadal oscillation and its relationship to rainfall and river flows in the continental U.S. *Geophys. Res. Lett.*, **28**, 2077–2080, <https://doi.org/10.1029/2000GL012745>.
- Fierro, A. O., 2014: Relationships between California rainfall variability and large-scale climate drivers. *Int. J. Climatol.*, **34**, 3626–3640, <https://doi.org/10.1002/joc.4112>.
- Gershunov, A., and T. P. Barnett, 1998: Interdecadal modulation of ENSO teleconnections. *Bull. Amer. Meteor. Soc.*, **79**, 2715–2725, [https://doi.org/10.1175/1520-0477\(1998\)079<2715:IMOET>2.0.CO;2](https://doi.org/10.1175/1520-0477(1998)079<2715:IMOET>2.0.CO;2).
- Gray, L. J., and Coauthors, 2010: Solar influences on climate. *Rev. Geophys.*, **48**, RG4001, <https://doi.org/10.1029/2009RG000282>.
- Guttman, N. B., and R. G. Quayle, 1996: A historical perspective of U.S. climate divisions. *Bull. Amer. Meteor. Soc.*, **77**, 293–303, [https://doi.org/10.1175/1520-0477\(1996\)077<0293:AHPOUC>2.0.CO;2](https://doi.org/10.1175/1520-0477(1996)077<0293:AHPOUC>2.0.CO;2).
- Herring, S. C., M. P. Hoerling, T. C. Peterson, and P. A. Stott, 2014: Explaining extreme events of 2013 from a climate perspective. *Bull. Amer. Meteor. Soc.*, **95** (9), S1–S96, <https://doi.org/10.1175/1520-0477-95.9.S1.1>.
- Higgins, R. W., A. Leetmaa, Y. Xue, and A. Barnston, 2000: Dominant factors influencing the seasonal predictability of U.S. precipitation and surface air temperature. *J. Climate*, **13**, 3994–4017, [https://doi.org/10.1175/1520-0442\(2000\)013<3994:DFITSP>2.0.CO;2](https://doi.org/10.1175/1520-0442(2000)013<3994:DFITSP>2.0.CO;2).
- , V. B. S. Silva, W. Shi, and J. Larson, 2007: Relationships between climate variability and fluctuations in daily precipitation over the United States. *J. Climate*, **20**, 3561–3579, <https://doi.org/10.1175/JCLI4196.1>.
- Hoell, A., M. Hoerling, J. Eischeid, K. Wolter, R. Dole, J. Perlwitz, T. Xu, and L. Cheng, 2016: Does El Niño intensity matter for California precipitation? *Geophys. Res. Lett.*, **43**, 819–825, <https://doi.org/10.1002/2015GL067102>.
- Hurrell, J. W., and H. van Loon, 1997: Decadal variations in climate associated with the North Atlantic Oscillation. *Climatic Change*, **36**, 301–326, <https://doi.org/10.1023/A:1005314315270>.
- Jones, C., 2000: Occurrence of extreme precipitation events in California and relationships with the Madden–Julian oscillation. *J. Climate*, **13**, 3576–3587, [https://doi.org/10.1175/1520-0442\(2000\)013<3576:OEOPEI>2.0.CO;2](https://doi.org/10.1175/1520-0442(2000)013<3576:OEOPEI>2.0.CO;2).
- Kalnay, E., and Coauthors, 1996: The NCEP/NCAR 40-Year Reanalysis Project. *Bull. Amer. Meteor. Soc.*, **77**, 437–470, [https://doi.org/10.1175/1520-0477\(1996\)077<0437:TNYRP>2.0.CO;2](https://doi.org/10.1175/1520-0477(1996)077<0437:TNYRP>2.0.CO;2).
- Kam, J., and J. Sheffield, 2016: Increased drought and pluvial risk over California due to changing oceanic conditions. *J. Climate*, **29**, 8269–8279, <https://doi.org/10.1175/JCLI-D-15-0879.1>.
- Langford, S., S. Stevenson, and D. Noone, 2014: Analysis of low-frequency precipitation variability in CMIP5 historical simulations for southwestern North America. *J. Climate*, **27**, 2735–2756, <https://doi.org/10.1175/JCLI-D-13-00317.1>.
- Li, J., and B. Wang, 2016: How predictable is the anomaly pattern of the Indian summer rainfall? *Climate Dyn.*, **46**, 2847–2861, <https://doi.org/10.1007/s00382-015-2735-6>.
- , and —, 2018: Predictability of summer extreme precipitation days over eastern China. *Climate Dyn.*, <https://doi.org/10.1007/s00382-017-3848-x>, in press.
- , —, and Y.-M. Yang, 2017: Retrospective seasonal prediction of summer monsoon rainfall over west central and peninsular India in the past 142 years. *Climate Dyn.*, **48**, 2581–2596, <https://doi.org/10.1007/s00382-016-3225-1>.
- Liu, X., X. Ren, and X.-Q. Yang, 2016: Decadal changes in multiscale water vapor transport and atmospheric river associated with the Pacific decadal oscillation and the North Pacific Gyre Oscillation. *J. Hydrometeorol.*, **17**, 273–285, <https://doi.org/10.1175/JHM-D-14-0195.1>.
- Luo, X., and B. Wang, 2017: How predictable is the winter extremely cold days over temperate East Asia? *Climate Dyn.*, **48**, 2557–2568, <https://doi.org/10.1007/s00382-016-3222-4>.
- , and —, 2018: Predictability and prediction of the total number of winter extremely cold days over China. *Climate Dyn.*, <https://doi.org/10.1007/s00382-017-3720-z>, in press.
- Maliniemi, V., T. Asikainen, and K. Mursula, 2014: Spatial distribution of Northern Hemisphere winter temperatures during different phases of the solar cycle. *J. Geophys. Res. Atmos.*, **119**, 9752–9764, <https://doi.org/10.1002/2013JD021343>.
- Mantua, N. J., S. R. Hare, Y. Zhang, J. M. Wallace, and R. C. Francis, 1997: A Pacific interdecadal climate oscillation with impacts on salmon production. *Bull. Amer. Meteor. Soc.*, **78**, 1069–1079, [https://doi.org/10.1175/1520-0477\(1997\)078<1069:APICOW>2.0.CO;2](https://doi.org/10.1175/1520-0477(1997)078<1069:APICOW>2.0.CO;2).
- McAfee, S. A., and J. L. Russell, 2008: Northern annular mode impact on spring climate in the western United States. *Geophys. Res. Lett.*, **35**, L17701, <https://doi.org/10.1029/2008GL034828>.
- McCabe, G. J., and M. D. Dettinger, 1999: Decadal variations in the strength of ENSO teleconnection with precipitation in the western United States. *Int. J. Climatol.*, **19**, 1399–1410, [https://doi.org/10.1002/\(SICI\)1097-0088\(19991115\)19:13<1399::AID-JOC457>3.0.CO;2-A](https://doi.org/10.1002/(SICI)1097-0088(19991115)19:13<1399::AID-JOC457>3.0.CO;2-A).
- McCabe-Glynn, S., K. R. Johnson, C. Strong, Y. Zou, J.-Y. Yu, S. Sellars, and J. M. Welker, 2016: Isotopic signature of extreme precipitation events in the western U.S. and associated phases of Arctic and tropical climate modes. *J. Geophys. Res. Atmos.*, **121**, 8913–8924, <https://doi.org/10.1002/2016JD025524>.
- Mills, C. M., and J. E. Walsh, 2013: Seasonal variation and spatial patterns of the atmospheric component of the Pacific decadal oscillation. *J. Climate*, **26**, 1575–1594, <https://doi.org/10.1175/JCLI-D-12-00264.1>.
- Mo, K. C., and R. W. Higgins, 1998: Tropical influences on California precipitation. *J. Climate*, **11**, 412–430, [https://doi.org/10.1175/1520-0442\(1998\)011<0412:TIOCP>2.0.CO;2](https://doi.org/10.1175/1520-0442(1998)011<0412:TIOCP>2.0.CO;2).
- , J.-K. E. Schemm, and S.-H. Yoo, 2009: Influence of ENSO and the Atlantic multidecadal oscillation on drought over the United States. *J. Climate*, **22**, 5962–5982, <https://doi.org/10.1175/2009JCLI2966.1>.

- Myoung, B., S. H. Kim, J. Kim, and M. C. Kafatos, 2015: On the relationship between the North Atlantic Oscillation and early warm season temperatures in the southwestern United States. *J. Climate*, **28**, 5683–5698, <https://doi.org/10.1175/JCLI-D-14-00521.1>.
- , —, —, and —, 2017: On the relationship between spring NAO and snowmelt in the upper southwestern United States. *J. Climate*, **30**, 5141–5149, <https://doi.org/10.1175/JCLI-D-16-0239.1>.
- Newman, M., and Coauthors, 2016: The Pacific decadal oscillation, revisited. *J. Climate*, **29**, 4399–4427, <https://doi.org/10.1175/JCLI-D-15-0508.1>.
- Panagiotopoulos, F., M. Shahgedanova, and D. Stephenson, 2002: A review of Northern Hemisphere winter-time teleconnection patterns. *J. Phys. IV*, **12**, 1027–1047.
- Rossow, W. B., and A. A. Lacis, 1990: Global, seasonal cloud variations from satellite radiance measurements. Part II. Cloud properties and radiative effects. *J. Climate*, **3**, 1204–1253, [https://doi.org/10.1175/1520-0442\(1990\)003<1204:GSCVFS>2.0.CO;2](https://doi.org/10.1175/1520-0442(1990)003<1204:GSCVFS>2.0.CO;2).
- , and Y.-C. Zhang, 1995: Calculation of surface and top of atmosphere radiative fluxes from physical quantities based on ISCCP data sets: 2. Validation and first results. *J. Geophys. Res.*, **100**, 1167–1197, <https://doi.org/10.1029/94JD02746>.
- Schlesinger, M. E., and N. Ramankutty, 1994: An oscillation in the global climate system of period 65–70 years. *Nature*, **367**, 723–726, <https://doi.org/10.1038/367723a0>.
- Schonher, T., and S. E. Nicholson, 1989: The relationship between California rainfall and ENSO events. *J. Climate*, **2**, 1258–1269, [https://doi.org/10.1175/1520-0442\(1989\)002<1258:TRBCRA>2.0.CO;2](https://doi.org/10.1175/1520-0442(1989)002<1258:TRBCRA>2.0.CO;2).
- Thompson, D. W. J., and J. M. Wallace, 1998: The Arctic Oscillation signature in the wintertime geopotential height and temperature fields. *Geophys. Res. Lett.*, **25**, 1297–1300, <https://doi.org/10.1029/98GL00950>.
- Tootle, G. A., and T. C. Piechota, 2006: Relationships between Pacific and Atlantic Ocean sea surface temperatures and U.S. streamflow variability. *Water Resour. Res.*, **42**, W07411, <https://doi.org/10.1029/2005WR004184>.
- Torrence, C., and G. P. Compo, 1998: A practical guide to wavelet analysis. *Bull. Amer. Meteor. Soc.*, **79**, 61–78, [https://doi.org/10.1175/1520-0477\(1998\)079<0061:APGTWA>2.0.CO;2](https://doi.org/10.1175/1520-0477(1998)079<0061:APGTWA>2.0.CO;2).
- Trenberth, K. E., 1984: Signal versus noise in the Southern Oscillation. *Mon. Wea. Rev.*, **112**, 326–332, [https://doi.org/10.1175/1520-0493\(1984\)112<0326:SVNITS>2.0.CO;2](https://doi.org/10.1175/1520-0493(1984)112<0326:SVNITS>2.0.CO;2).
- , and J. W. Hurrell, 1994: Decadal atmosphere–ocean variations in the Pacific. *Climate Dyn.*, **9**, 303–319, <https://doi.org/10.1007/BF00204745>.
- , and D. P. Stepaniak, 2001: Indices of El Niño evolution. *J. Climate*, **14**, 1697–1701, [https://doi.org/10.1175/1520-0442\(2001\)014<1697:LIOENO>2.0.CO;2](https://doi.org/10.1175/1520-0442(2001)014<1697:LIOENO>2.0.CO;2).
- Wang, B., B. Xiang, J. Li, P. J. Webster, M. N. Rajeevan, J. Liu, and K.-J. Ha, 2015: Rethinking Indian monsoon rainfall prediction in the context of recent global warming. *Nat. Commun.*, **6**, 7154, <https://doi.org/10.1038/ncomms8154>.
- Wang, C., and D. B. Enfield, 2001: The tropical Western Hemisphere warm pool. *Geophys. Res. Lett.*, **28**, 1635–1638, <https://doi.org/10.1029/2000GL011763>.
- Wang, S.-Y., L. Hips, R. R. Gillies, and J.-H. Yoon, 2014: Probable causes of the abnormal ridge accompanying the 2013–2014 California drought: ENSO precursor and anthropogenic warming footprint. *Geophys. Res. Lett.*, **41**, 3220–3226, <https://doi.org/10.1002/2014GL059748>.
- Weng, H., K. Ashok, S. K. Behera, S. A. Rao, and T. Yamagata, 2007: Impacts of recent El Niño Modoki on dry/wet conditions in the Pacific Rim during boreal summer. *Climate Dyn.*, **29**, 113–129, <https://doi.org/10.1007/s00382-007-0234-0>.
- , S. K. Behera, and T. Yamagata, 2009: Anomalous winter climate conditions in the Pacific Rim during recent El Niño Modoki and El Niño events. *Climate Dyn.*, **32**, 663–674, <https://doi.org/10.1007/s00382-008-0394-6>.
- Wettstein, J. J., and J. M. Wallace, 2010: Observed patterns of month-to-month storm-track variability and their relationship to the background flow. *J. Atmos. Sci.*, **67**, 1420–1437, <https://doi.org/10.1175/2009JAS3194.1>.
- Whan, K., and F. Zwiers, 2017: The impact of ENSO and the NAO on extreme winter precipitation in North America in observations and regional climate models. *Climate Dyn.*, **48**, 1401–1411, <https://doi.org/10.1007/s00382-016-3148-x>.
- Wilks, D. S., 2006: *Statistical Methods in the Atmospheric Sciences*. 2nd ed. International Geophysics Series, Vol. 100, Academic Press, 648 pp.
- Wise, E. K., 2010: Spatiotemporal variability of the precipitation dipole transition zone in the western United States. *Geophys. Res. Lett.*, **37**, L07706, <https://doi.org/10.1029/2009GL042193>.
- , M. L. Wrzesien, M. P. Dannenberg, and D. L. McGinnis, 2015: Cool-season precipitation patterns associated with teleconnection interactions in the United States. *J. Appl. Meteor. Climatol.*, **54**, 494–505, <https://doi.org/10.1175/JAMC-D-14-0040.1>.
- Wolter, K., and M. S. Timlin, 1993: Monitoring ENSO in COADS with a seasonally adjusted principal component index. *Proc. 17th Climate Diagnostics Workshop*, Norman, OK, NOAA/NMCC/CAC, 52–57, <https://www.esrl.noaa.gov/psd/ens/mei/WT1.pdf>.
- , and —, 1998: Measuring the strength of ENSO events: How does 1997/98 rank? *Weather*, **53**, 315–324, <https://doi.org/10.1002/j.1477-8696.1998.tb06408.x>.
- , and —, 2011: El Niño/Southern Oscillation behaviour since 1871 as diagnosed in an extended multivariate ENSO index (MEI.ext). *Int. J. Climatol.*, **31**, 1074–1087, <https://doi.org/10.1002/joc.2336>.
- Wu, L., F. He, Z. Liu, and C. Li, 2007: Atmospheric teleconnections of tropical Atlantic variability: Interhemispheric, tropical–extratropical, and cross-basin interactions. *J. Climate*, **20**, 856–870, <https://doi.org/10.1175/JCLI4019.1>.
- Yoon, J.-H., S.-Y. S. Wang, R. R. Gillies, B. Kravitz, L. Hips, and P. J. Rasch, 2015: Increasing water cycle extremes in California and in relation to ENSO cycle under global warming. *Nat. Commun.*, **6**, 8657, <https://doi.org/10.1038/ncomms9657>.
- Zhu, Z., and T. Li, 2016: A new paradigm for continental U.S. summer rainfall variability: Asia–North America teleconnection. *J. Climate*, **29**, 7313–7327, <https://doi.org/10.1175/JCLI-D-16-0137.1>.
- , and —, 2017a: The record-breaking hot summer in 2015 over Hawaii and its physical causes. *J. Climate*, **30**, 4253–4266, <https://doi.org/10.1175/JCLI-D-16-0438.1>.
- , and —, 2017b: Empirical prediction of the onset dates of South China Sea summer monsoon. *Climate Dyn.*, **48**, 1633–1645, <https://doi.org/10.1007/s00382-016-3164-x>.
- , and —, 2018: Amplified contiguous United States summer rainfall variability induced by East Asian monsoon interdecadal change. *Climate Dyn.*, <https://doi.org/10.1007/s00382-017-3821-8>, in press.